Supplementary Online Content

Verma R, Swanson RL, Parker D, et al. Neuroimaging findings in US government personnel with possible exposure to directional phenomena in Havana, Cuba [published July 23, 2019]. *JAMA*. doi:10.1001/jama.2019.9269

This supplementary material has been provided by the authors to give readers additional information about their work.

Elements: eAppendixes and associated Tables and Figures

eAppendix 9: Additional functional connectivity analysis

9.1 Comparison of functional connectomes (associated eFigure 18)

9.2 Analysis after removing the PBI cohort (associated eFigure 19)

eAppendix 10: Analysis of WM hyperintensities

eAppendix 11: Additional results of correlation of clinical scores with imaging (associated eTables 6 and 7, and eFigure 20)

Abbreviations:

DTI: Diffusion Tensor Imaging

MRI: Magnetic Resonance Imaging

dMRI: diffusion MRI

rs-fMRI: resting state functional MRI

FA: Fractional Anisotropy

MD: Mean Diffusivity

AD: Axial Diffusivity

RAD: Radial Diffusivity

VF: Volume fraction

FDR: False Discovery Rate

WM: White matter

GM: Grey matter

CSF: Cerebrospinal fluid

PBI: Prior Brain Injury

USG: United States Government

QC: Quality control

ROI: Region of Interest

The neuroimaging data were acquired on the USG cohort (henceforth referred to as "patients") to develop diagnostic criteria for a potentially novel neurological syndrome.

eAppendix 1. Acquisition details

The imaging protocol for the patients: 1) a clinical T2 (TR=3.2 sec, TE=0.564 sec, FOV=166 x 240 mm, number of slices = 320, voxel dimension = 0.8 x 0.8 x 0.8 mm^3). 2) 3D FLAIR (TR=6.00 sec, TE=.286 sec, FOV=160 x 220 mm, number of slices = 256, voxel dimension = 1.0 x 1.007812 x 1.007812 mm^3). 3) T1 (9 patients (TR=1.82 sec, TE=0.0053 sec, Inversion Time= 1.1 sec, FOV = 160x256 mm, number of slices = 160, voxel dimension = 0.9375 x 0.9375 x 1 mm^3) and 21 patients (TR=1.82 sec, TE=0.00353 sec, Inversion Time= 1.1 sec, FOV = 256x256 mm, number of slices = 256, voxel dimension = 1 x 1.015625 x 1.015625 mm^3). 4) Multishell multiband dMRI (TR=4.3 sec, TE=0.075 sec, FOV = 220x220 mm, number of slices = 76, voxel dimension = 2 x 2 x 2 mm^3, 109 gradient directions with shells corresponding to b=300, 800, 2000 s/mm^2 with 15, 30 and 64 gradient directions, respectively and 9 non-diffusion weighted b0 acquisitions). We used a multiband acceleration [1] (MB factor=2) to reduce the acquisition time. 5) Resting state fMRI (rs-fMRI) (TR=0.5 sec, TE=0.03 sec, FOV = 192x192 mm, number of slices = 48, voxel dimension = 3 x 3 x 3 mm^3, number of volumes = 742).

The imaging protocol for the control set 1: 1) FLAIR (TR=6.00 sec, TE=.286 sec, FOV=160 x 220 mm, number of slices = 256, voxel dimension = 1.0 x 1.007812 x 1.007812 mm^3). 2) T1 (TR=1.82 sec, TE=0.0053 sec, Inversion Time= 1.1 sec, FOV = 180x240 mm, number of slices = 160, voxel dimension = 0.9375 x 0.9375 x 1 mm^3). 3) Multishell multiband dMRI (TR=4.3 sec, TE=0.075 sec, FOV = 220x220 mm, number of slices = 76, voxel dimension = 2 x 2 x 2 mm^3, 109 gradient directions with shells corresponding to b=300, 800, 2000 s/mm^2 with 15, 30 and 64 gradient directions, respectively and 9 non-diffusion weighted b0 acquisitions). We used a multiband acceleration [1] (MB factor=2) to reduce the acquisition time. 4) Resting state fMRI (rs-fMRI) (TR=0.5 sec, TE=0.03 sec, FOV = 192x192 mm, number of slices = 48, voxel dimension = 3 x 3 x 3 mm^3, number of volumes = 742).

The imaging protocol for control set 2: 1) T1 (TR=1.62 sec, TE=0.003 sec, Inversion Time= 0.95 sec, FOV = 192 x 256 mm, number of slices = 160, voxel dimension = 1 x 1 x 1 mm^3). 2) DTI (TR=6.5 sec, TE=0.084 sec, FOV = 245 x 245 mm, number of slices = 57, voxel dimension = 2.2 x 2.2 x 2.2 mm^3, 30 gradient directions at b=1000 s/mm^2, repeated twice, and 7 non-diffusion weighted b0 acquisitions, acquired twice consecutively).

eAppendix 2. QC and processing pipelines for imaging data

Quality control (QC) and processing pipelines consisting of extensively validated methods were applied for processing the different MRI modalities. These pipelines have been developed in-house and improved over several years and applied to large studies in aging [2-7], autism [8-10], psychopathology [11] and development [12], traumatic brain injury [13, 14], brain tumors [15] and others [16, 17].

Structural MRI (T1) pipeline: Inhomogeneity correction was performed using N3 bias field correction [18] on the raw, non-skull stripped T1 images of the BND, and control cohorts. Skull stripping and segmentation of the brain volumes into GM, WM and CSF was achieved using MUSE (Multi-atlas region Segmentation utilizing Ensembles of registration algorithms and parameters) [19].

Diffusion MRI pipeline: We applied a stringent semi-automated QC pipeline to detect artifacts and outliers. As a first step, it was checked that the field of view encompasses the full brain, and the scanning parameters (TR, TE, voxel dimensions) match across the study. Then each dMRI volume was visually inspected for ghosting, signal dropout (detectable as a black line across the brain), signal spikes (detectable as a bright line), venetian blind, motion artifacts, multi-band and unclassifiable artifacts. If more than 10% of volumes had artifacts, the entire scan was rejected; otherwise, those gradient images were removed from the volume. We then applied our in-house processing pipeline which includes noise removal with a local PCA method [20] that utilizes the 4D nature of diffusion data, correction for participant motion and eddy current deformations using FSL's eddy [21, 22], extraction of the mean b0 image and estimation of a brain mask using FSL's BET [23].

fMRI pipeline: Resting state fMRI data was processed per [24].

eAppendix 3. Creation of Imaging Measures

3.1 Volumetric measures: In our voxel-wise volumetric analyses, we used regional volumetric maps, named RAVENS (Regional Analysis of Volumes Examined in Normalized Space) maps [25, 26]. RAVENS map intensity values quantify the regional distribution of GM, WM and CSF, with one RAVENS map for each tissue type. In particular, RAVENS values in the template space are directly proportional to the volume of the respective structures in the original brain scan. The RAVENS approach has been extensively used and validated in large-scale neuroimaging studies [27-29]. In order to achieve optimal consistency between regional volumetric and voxel-wise analyses across multiple scanners and scanning protocols, we used a region of interest (ROI) based segmentation approach in the calculation of RAVENS maps, instead of an intensity-based tissue segmentation. To do this, anatomical regions of interest (ROIs) were first segmented on the T1-weighted scan of each subject using the MUSE (Multi-atlas region Segmentation utilizing Ensembles of registration algorithms and parameters) anatomical labeling approach [19]. MUSE is a consensus labeling framework, which generates an ensemble of labeled atlases in target image space via the use of several registration algorithms, regularization parameters, and atlases. Each registration from the ensemble yields different solutions, providing complementary information to MUSE's final 'label-fusion' step. The 'label-fusion' step uses a local similarity ranking and a boundary modulation term, to refine the segmentation. The tissue type of each ROI was then used to segment the brain into GM, WM and CSF. For subject to template warping, we used a deformable registration method, DRAMMS [30], to compute the final RAVENS-MUSE maps. The RAVENS-MUSE maps were then normalized by the intracranial volume (ICV) of each scan to control for inter-subject differences in head size and smoothed using a 4 mm isotropic Gaussian kernel.

3.2 Measures of microstructural tissue integrity and connectivity: Diffusion MRI (dMRI) [31] is an MRI modality that uses recorded signals from various weighted and unweighted gradients to characterize the diffusion behavior of water molecules within a given voxel. While the signals from the unweighted directions provide a T2-like reference contrast, the recorded readings from the weighted gradients are particularly interesting as they vary greatly despite applying re-phasing gradients that are equivalent in magnitude to the dephasing ones. This phenomenon has been attributed to the diffusion properties of the environment of interest and is utilized clinically to investigate WM structures non-invasively. One of the most popular frameworks in the clinical practice to infer the diffusion behavior from dMRI data is Diffusion Tensor Imaging (DTI) [32-34].

A tensor can be thought of as an ellipsoidal object that describes the diffusion behavior through its geometrical properties such as its shape and volume, using the magnitude of its long axis and two short axes (eFigure1A). The axes are described by three vectors known as eigenvectors with eigenvalues ($\lambda_1, \lambda_2, \lambda_3$) that correspond to their magnitudes. The eigenvalues are used to create various DTI indices: The magnitude (λ_1) of the long axis describes the axial diffusivity (AD), while the average length of the two short axes (λ_2 and λ_3) is known as the radial diffusivity (RAD) (eFigure1A). The mean diffusivity (MD) is the average of the three eigenvalues, while the fractional anisotropy (FA) is a mathematical formula that describes the diffusion asymmetry in the tensor (eFigure1A). As such, an isotropic (low FA) tensor with a large MD would signify the diffusion in freely diffusing regions (e.g., CSF) (eFigure1B-C), an isotropic tensor with relatively lower MD would be describing a typical GM voxel (eFigure1B-C), and an anisotropic tensor (high FA) with relatively a lower MD would present regions such as the genu of the corpus callosum (eFigure1B-C). As such, these diffusion tensor indices can provide useful tissue contrast [35]. MD is higher in CSF than tissue, and MD in GM is slightly higher than WM. FA is higher in WM compared to other tissue types, due to the restrictive nature of coherent axonal bundles. While FA is highly sensitive to change, it is not specific whether the change in FA is as a result of AD or RAD variation. Multicompartment modeling of the tensor model is used to obtain the free water volume fraction [36, 37]. FA, RAD and AD are more sensitive to changes in the WM, while MD is more sensitive in the GM, but may be used in the WM as well as it is indicative of the increase or decrease of free water. VF can be used in the whole brain to estimate the extent of inflammation causing pathologies. These measures give rise to different contrasts based on modeling the signal to describe some microstructural properties of interest such as the changes in intra- and extracellular compartments. A combination of these measures (the direction of differences when compared to controls) may be indicative of different axonal and myelin processes and are used to interrogate pathology induced change in different clinical studies. These have also been shown in eFigure 2.

A combination of increase and decrease in these measures, in patients compared to controls, has previously been used to evaluate several pathologies, such as traumatic brain injury (TBI) [38, 39], multiple sclerosis [40, 41], aging [42, 43], schizophrenia and psychopathology [44-46], neoplasia [37], and acute and chronic stroke [47]. Notably, concussion and/or mild TBI in the acute stages show a decrease in MD and increase in FA, which is in the opposite direction for more severe TBI [48].

DTI uniquely provides information about fiber orientation (given by the orientation of the fitted ellipsoid), and various methods of tractography can be used to follow the fiber orientation between regions. The eigenvector corresponding to the highest magnitude eigenvalue in the diffusion tensor is known as the principal direction and is used for tractography [49, 50]. Streamlines are generated by following the principal direction through the brain, in the WM regions, based on an FA threshold. These streamlines connect various regions of the brain. In order to create a structural connectome, the brain is parcellated into regions based on an atlas of choice. Tractography between these regions is used to quantify connectivity, leading to a graph representation of connections in the brain (eFigure1D) [51, 52]. The brain graph can be divided to subnetworks that are meaningful in a structural or functional context and may bring insight into various pathologies.

The dMRI data from the 800 shell was used for creating the DTI indices and for free water estimation , while the 800 and 2000 shells were used for probabilistic tractography. The QC-ed and processed data (as explained in eAppendix 2) were fitted with tensors [53] using weighted linear fitting, and the diffusion indices of FA, MD, RAD and AD representing underlying microstructural tissue integrity were computed, using DIPY tools [54]. The free water volume fraction (VF) map was obtained by fitting a bi-compartment model using [37]. In order to create the connectomes, we parcellated the brain using a modified version of the Lausanne atlas [55] using Freesurfer on the T1 and a python post-processing step called "easy_lausanne", further parcellating the cerebellum into 8 nodes per hemisphere based on the Yeo parcellation of the cerebellum [56], and parcellating the brain stem into 3 nodes (brain stem, superior colliculus left and superior colliculus right) using ROIs drawn on the JHU template and registered to each subject's T1 using ANTs [57, 58]. The final modified Lausanne atlas consisted of 252 regions. We used probabilistic tractography (probtrackx from FSL [59]) to obtain streamlines connecting pairs of regions in the parcellation [21, 59] (dMRI data from the 800 and 2000 shells were used for probabilistic tractography). A 252 x 252 adjacency matrix was calculated using the streamline count between regions, called the *structural connectome.*

3.3 fMRI connectomes and subnetworks: 90 ROIs for the Greicius FMRI atlas [60] were warped to the space of the JHU (Eve) atlas [61, 62] and from there to each subject's T1 via nonlinear warping with ANTs registration [57, 58]. 6 of the 90 ROIs proved to be too small for analysis, as the ROIs after the warping process were not present in every subject. Those 6 ROIs were each less than 160 mm^3 in volume in the original atlas. The warping process left 84 ROIs in each subject for subsequent analysis. Timeseries were calculated for each of the 84 regions and an 84 x 84 adjacency matrix, called the *functional connectome*, was calculated from the Pearson correlation coefficient of the timeseries for each pair of regions. Edges represented by negative correlation values were set to zero. All edges were collected for each pair of regions in the visuospatial subnetwork of the atlas, consisting of 11 ROIs, for a total of 55 edges, and the mean was taken to produce one visuospatial subnetwork measurement for each subject. The same was performed for the Auditory network (3 ROIs) and the Executive Control network (the union of the Left Executive Control Network and Right Executive Control Network in the original atlas, consisting of 11 ROIs). eTable 4 shows the regions involved in the Auditory and Visuospatial subnetworks.

eAppendix 4: Combination of control cohorts

Volumetric maps: As the data has been corrected for inhomogeneity, the volumetric maps created were independent of the actual acquisition. The maps were statistically tested for differences using the same tests as used for the patients. There were no significant differences, hence the two groups were combined.

Tissue integrity: DTI maps of FA, MD, AD, RAD, and VF from free-water elimination, were smoothed in template space within a mask of brain tissue (excluding ventricles and CSF) using Gaussian kernels of 8 mm full-width-at-half-maximum for the 5 measures. Subsequently, ComBat [63] was applied to harmonize the data from the second cohort of controls to the first cohort by eliminating scanner effects while retaining effects associated with variables of outcome (patient or control), age, and sex, resulting in smoothed, harmonized maps for voxels within the GM and WM masks of the template.

ComBat is a tool for reducing systematic biases across acquisition batches developed for gene expression studies that has been shown to be effective for removing site and scanner effects from diffusion, volumetric, and other neuroimaging data, while preserving biological associations. The ComBat model allows for mean and variance differences across scanners, drawing strength across measurements within an empirical Bayesian framework to estimate and remove these biases. Software for conducting ComBat harmonization is available for download at https://github.com/Jfortin1/ComBatHarmonization.

eAppendix 5: Additional analysis of volumetric maps

5.1 Voxel-wise volumetric analysis: Volume map residuals were found to be normally distributed within groups by the Anderson-Darling test of normality in GM and WM voxels. As can be seen in Fig. 1, there were widespread volume differences in the brains of the patients compared to the controls, both in WM and GM. These differences form an unusual pattern of higher WM volume in the projection fibers (especially corona radiata and the internal capsule), and lower WM volume in the association fibers (also called U-fibers). The commissural fibers showed a mixed pattern of lower volume in the genu and body and higher volume in the splenium of the corpus callosum. GM volume was lower in the cortex and thalamus. In the cerebellum of the patients, the superficial cerebellar GM showed higher volume, with the deep GM and neighboring WM showing lower volumes, as compared to controls.

The volumetric analysis was repeated with a 2mm and an 8mm kernel of smoothing. The results showed significant difference in the same regions. The analysis was also repeated using two different inhomogeneity corrections N3 and N4 [64], with the areas of significant differences being similar between the corrections. The analysis was also repeated by combining the WM and GM tissue, to ensure that the effect we are seeing is not due to registration. The results remained the same in terms of the areas of significant differences.

5.2 Region-wise differences in tissue volume: The volume maps of patients and controls, were normalized to the space of the Neuromorphometrics Atlas [65]. Average GM and WM volume were created for each of the ROIs. Group difference between the patients and the controls was assessed statistically using the same model as was used for the voxel-wise analysis. The differences were controlled for age, sex and (ICV. eFigure 3 shows some of the regions of significant difference.

5.3 Analysis on excluding the PBI cohort: We analyzed the patients with and without the PBI cohort (patients who had some prior history of brain injury, resolved prior to the reported exposure). eFigure 4 shows the results of analysis. These statistically unthresholded results show that the differences are in the same regions and direction. This suggests that the differences observed in the full sample of patients, as compared to controls, was not due to pre-existing conditions in a small subgroup of subjects.

5.4 Comparison of the patients with different control cohorts: The volumetric analysis was repeated by comparing the patients to each of the control groups (sets 1 and 2), separately and combined. eFigure 5 shows the results in the case of WM volume maps. As can be seen, the direction of differences in the comparison of the patients to the two control groups, separately and combined, remains the same, with very similar effect sizes, and similar regions showing differences. The uncorrected differences between the WM maps of the two control groups show a reversed direction of differences than the analysis in columns 1, 2, and 3, showing that differences in controls do not drive the differences seen in the patients. These differences between control cohorts do not survive multiple comparisons correction. Similar results were obtained for GM maps, as well as the targeted analysis of the cerebellum. Thus, we have been able to replicate the analysis in two control cohorts with different demographics, showing that the results seen in the patients are not as a result of a specific control cohort.

5.5 Percentage change in volume: Volume differences can also be represented as a map of percentage volume change, computed between the average of the patients, compared to their controls. eFigure 6 shows representative slices from the percentage volume change maps for the voxels that were shown to be significantly different between patients and controls. It may be noted that these differences are at the voxel level which is 1mm in dimension. Thus, these differences are not visible to the naked eye and require advanced voxel-based statistical analysis of volumes to detect.

5.6 Adjustment for intra-cranial volume: RAVENS-MUSE uses ICV for voxel-wise normalization, which could be thought to bias the results. Thus, the analysis was repeated by removing the voxel-wise normalization and used ICV as a covariate (keeping all else the same in the statistical analysis), and the results did not change. Additionally, we undertook the allometric analysis as described in [66], with no change in the pattern of differences between the patients and the controls.

5.7 Handling changes in protocol and methodological variation: As is common in t clinical acquisitions, there were inadvertent head coil changes or small changes in scanner parameters, where the effect of the inhomogeneity is uncharacterized. This was handled in different ways: 1) Each image was manually inspected after correction to make sure that the correction was uniformly applied. 2) All analyses were repeated with different bias field corrections, to ensure that the results remained the same. 3) The comparison was repeated with each of the control groups independently (see eAppendix 5.2) leading to the same results, while there was no significant difference between the control groups. 4) Methodological variations were tested by applying SPM-CAT12 (see eAppendix 6 for details) and getting compatible

results, albeit less sensitive, as expected due to the method's inferior accuracy. In the past 5 years, multi-atlas segmentation methods have been widely shown to perform significantly better by virtue of using a diverse set of atlases and an intelligent voting process, which cancels out random labeling errors. In addition, it adaptively chooses the optimal templates that match regional anatomy. The RAVENS-MUSE segmentation used in this paper has won the MICCAI 2013 Challenge Workshop on Segmentation and is still ranked the highest despite additional submissions over the years.

eAppendix 6: Comparison of methods for volumetric analysis: RAVENS-MUSE and SPM-CAT12 pipelines

We will compare our RAVENS-MUSE pipeline used for volumetric analysis with the popular SPM-CAT12 pipelines for performing a statistical analysis of tissue volumes. These approaches comprise segmentation of the brain image into different tissue types, spatial normalization of the tissue maps into a stereotaxic atlas space, followed by a subsequent voxel-wise statistical analysis of the resulting spatial distributions of different tissue types. Both pipelines perform the aforementioned bold-faced steps but using different image processing tools.

6.1 SPM-CAT12: This pipeline is dependent upon GUI-based MATLAB toolboxes SPM12 (Statistical Parametric Mapping 12), and CAT12 (Computational Anatomy Toolbox 12) [see CAT12 user manual for details: http://www.neuro.uni-jena.de/cat12/CAT12-Manual.pdf]. All raw T1 images were manually AC-PC (Anterior Commissure-Posterior Commissure) aligned. The data was then bias corrected and segmented using CAT12's 'Segment Data' module into 6 probability maps (GM, WM, CSF, soft tissue, skull/bone, and background voxels) in MNI152 space, based on the SPM12 toolbox's Tissue Probability Map. The resultant spatially normalized GM, WM, & CSF segmentation probability maps were 'modulated' by multiplying them with the Jacobian determinant. The modulated and spatially normalized GM maps were then smoothed using SPM12's 'Smooth' module. While the default option of SPM12 is 8mm, analysis was repeated using 4mm. A two-sample t-test between patients and controls was run on the smoothed, modulated and spatially normalized GM maps, using CAT12's 'Basic Models' module. Total intracranial volume, as estimated in the 'Segment' module, was used as a covariate along with age and sex. As the SPM12 and CAT12 toolboxes do not have an appropriate tissue probability map for WM, analysis was restricted to the GM. It was also noted on the CAT12 webpage that the VBM analysis lacked sensitivity in studying WM volume differences, and that more appropriate methods such as DTI should be used for such analyses.

6.2 RAVENS-MUSE: This pipeline utilized MUSE (Multi-atlas region Segmentation utilizing Ensembles of registration algorithms and parameters), a multi-atlas segmentation tool, and RAVENS (Regional Analysis of Volumes Examined in Normalized Space), a tool used to characterize regional atrophy in the brain. While this has been discussed in eAppendix 5.1, the details are repeated here to provide a step-by-step comparison of pipelines. Inhomogeneity correction was performed twice on all raw T1 images from both groups using the N3 tool. Bias corrected images were then skull-stripped using MUSE, which registers 11 closely matching template images (from a library of 216 template images and their corresponding ground truth brain masks) to each brain volume to using two different non-linear registration algorithms (ANTs & DRAMMS). The resulting ensemble of labels are then fused in the target image space to achieve the final brain mask. MUSE was then run on the skull-stripped images to segment the brain into 153 anatomical regions of interest (ROIs), using a library of 35 template images with their corresponding labels. These ROIs were then fused together based on their underlying tissue type to achieve a tissue segmentation into GM, WM, ventricle and CSF regions. Deformation fields were generated using DRAMMS between the JHU-MNI-ss (Eve) Template [67] and each skull-stripped brain image, which were used to create tissue density maps (RAVENS maps), of the given subject, with respect to the template space. The RAVENS maps are usually normalized by ICV, but analysis was repeated using ICV as a covariate. The segmented, spatially normalized RAVENS maps were smoothed with a 4mm FWHM Gaussian kernel. Analysis was repeated with 2mm and 8mm kernels. A two-sample t-test was performed using '3dttest' from the AFNI suite (Analysis of Functional Neuroimages) for each tissue type. ICV (estimated from the brain mask), sex, and age were used as covariates.

6.3 Comparison of Segmentation output: A major difference between the two pipelines lies in the algorithms used to segment the brain into different tissue classes. While the RAVENS-MUSE pipeline utilizes MUSE's consensus framework of multi-atlas registrations to segment each brain volume, the SPM-CAT12 pipeline relies on an initial segmentation estimate achieved using SPM's classical 'Unified Segmentation' approach [45], followed by subsequent Adaptive Maximum A Posteriori (AMAP) technique. The AMAP estimation models local variations of mean and variance, as slowly varying spatial functions [46]. The outcome of segmentation from the two pipelines, is displayed in eFigures 7 and 8. eFigure 7 displays how CAT12 under segments the superior cortical GM, while MUSE recovers these gyri. Additionally, the WM segmentation in CAT12 (eFigure 8) appears to infiltrate subcortical GM areas and

under segments the superior peripheral WM. MUSE, on the other hand, is capable of recovering the lost WM tissue, and also respects the WM-subcortical GM tissue boundaries (eFigure 8).

6.4 Results of SPM-CAT12 volumetric analysis: An identical statistical model was run on the smoothed, modulated gray matter images obtained from the SPM-CAT12 pipeline as was run on the RAVENS maps from the RAVENS-MUSE pipeline, using CAT12's 'Basic Models' module. As shown in eFigure 9 there is a decreased volume in the frontal lobe and superior parietal regions of the patients, as compared to their controls. In addition to this, an increase in deep cerebellar GM volume was seen in the patients compared to controls. All results are reported after clusterizing at 100 voxels (1.5 mm isotropic) and correcting for family-wise error rate (FWE 0.05). By visually comparing these results to those in from the RAVENS-MUSE pipeline (see Fig. 1), it can be seen that the aforementioned regions were also similarly affected in the RAVENS maps analysis. The additional regions that show up in the RAVENS analysis could be due to the segmentation issues of SPM and its inability to correct for bias.

Owing to the absence of an appropriate WM tissue probability map in the SPM12 and CAT12 toolkits, we do not have a comparison of SPM-CAT12's performance compared to the WM analysis in the RAVENS-MUSE pipeline. The manual recommends the use of DTI for this purpose or uses the GM tissue probability map to mediate the WM registration, which leads to erroneous results per our investigation.

eAppendix 7. Additional analysis of microstructural tissue integrity measures

7.1 Results of comparing RAD, AD and VF in the cerebellum of patients to controls: eFigures 10, 11 and 12 shows the results of comparing the AD, RAD and VF in the cerebellum of the patients as to the controls. As can be seen, AD, RAD and VF are significantly lower in the patients, and the regions with differences overlap with those observed in MD and FA (reported in the manuscript, Figure 3). Additional views for MD and FA are also shown in eFigure 21.

7.2 ROI analysis in the cerebellum: The cerebellum was parcellated into functionally-defined regions based on the Yeo atlas [56]. eFigure 13 shows the results of the analysis indicating a lower MD in the patients compared to the controls. eTable 5 provides the actual p-values of the regions. Regions showing significance, as well as trends are reported. Regions of increased FA are also reported in eTable 5.

7.3 Analysis after excluding of PBI cohort: Each of the diffusion indices were compared to the controls, before and after excluding the PBI cohort. As can be seen from eFigure 14, the direction and regions of difference remains the same in MD. The same was observed in the other measures of RAD, AD, FA and VF. There is a difference in effect size, as is expected. However, similar regions would be expected to survive multiple comparisons correction, as in the full cohort. This shows that the results observed in the patients are not a result of prior conditions in the subset of the cohort.

7.4 Comparison of the patients with different control cohorts: The analysis of the tissue integrity measures was repeated by comparing the patients to each of the control groups (sets 1 and 2), separately and combined. eFigure 15 shows the results in the case of MD. As can be seen, the direction and areas of differences in the comparison of the patients to the two control groups, separately and combined, remains the same, with very similar effect sizes. There are also no significant differences in the MD maps of the two control groups, supporting their combination. Similar results were obtained for AD, RAD, FA and VF. Thus, we have been able to replicate the analysis in two control cohorts with different demographics, demonstrating their consistency.

7.5 Comparison of results with and without ComBat harmonization: In order to ensure that the results seen in tissue integrity measures are not the result of harmonization, the patient versus control group 1 analysis was repeated with and without ComBat harmonization. As can be seen, in eFigure 16, the results are similar, although ComBat may introduce a smoothing, which is expected.

eAppendix 8: Structural connectivity analysis

eFigure 17 shows the results of comparing the structural connectomes of the patients with control set 1 at the level of each connection using Mann-Whitney U test. As each connectome was a 252 x 252 symmetric matrix, there were 31626 connections to be interrogated, and the ones represented in the figure did not survive multiple comparison correction. There wass no consistent trend of higher or lower connectivity in the patients compared to the controls, within and across hemisphere. This could be due to a combination of reasons; the streamline count that was used as a measure of connection strength was affected by the tracking algorithm, which in turn was affected by any change in

FA or VF, and the changes in the volume of the GM which was used for seeding the tracking. In addition, there were varied volumetric differences in projection, association and commissural fibers, which affected the connectivity. All these factors combined to alter the structural connectivity, which is reflected in the brain-wide differences seen in the figure, but do not form a coherent pattern of higher or lower in the patients as compared to controls. It also makes the sign of the difference (lower or higher) more challenging to interpret. The connections that show significant differences, do not consistently form a part of subnetworks. No correlation analysis was undertaken for structural connectivity as the differences did not demonstrate a coherent pattern.

eAppendix 9: fMRI connectivity analysis

9.1 Comparison of functional connectomes: Comparison of the full functional connectome of the patients compared to the control set 1, revealed connection difference that were widespread in the brain, as can be seen in eFigure 18 (top). These do not survive multiple comparison correction. In eFigure 18 (bottom), we analyzed the difference when the regions are grouped based on the subnetworks that they participate in. There was lower connectivity within each subnetwork of the patients compared to the controls, although group differences in connectivity across subnetworks may vary (lower/higher). The inter-subnetwork connectivity is challenging to interpret and hence, not investigated further.

9.2 Analysis after excluding the PBI cohort: eFigure 19 shows the results of the comparison of the subnetwork connectivity of patients with that of the controls, after excluding the PBI group. Comparison with Figure 3 in the manuscript shows that the direction of differences and the subnetworks affected (and their significance) remains the same. This indicates that the functional differences seen in the patients is not as a result of a pre-existing condition.

eAppendix 10: Analysis of WM hyperintensities

White matter hyperintensities, which were qualitatively described in the previous report [68], are used routinely in clinical evaluation to assess presence of abnormalities [69]. FLAIR and T2 weighted images for patients and control group 1 were assessed for WM hyperintensities by the neuroradiologist and graded by an ordinal scale with values as follows: [0 = none; 1 = mild, OK for age; 2 = mild, more than expected; 3 = moderate; 4 = marked]. This ordinal scale is based on the widely accepted Fazekas scale [70]. Such an ordinal scale is used in aging studies [71]. The controls were also evaluated qualitatively by the same radiologist to flag abnormalities and determine the appropriateness for inclusion. A Mann-Whitney U test run on the WM hyperintensity grades showed no significant group difference ($U=416.5$, $p=0.48$) between the patients and control set 1. It may be noted that only control set 1 was evaluated, because they had a protocol radiologically similar to the patients. No participant in either group received a grade of 4. No further analysis was undertaken on WM hyperintensities, as there was no hypothesis.

eAppendix 11: Additional results on correlation with clinical scores

Correlation of clinical scores with imaging requires quantitative measures of assessment that have been uniformly acquired on all patients, along with hypothesis-driven, specific brain regions. However, available data was generated as part of clinical evaluation and treatment and not a prospective research project. As reported previously [68], two of the most common clinical symptoms reported with corresponding objective findings were vestibular and oculomotor in nature. But since clinical indications guided sub-specialty referrals, quantitative clinical measures for vestibular and oculomotor function were not uniformly available for all patients. Correlations of neuroimaging findings with clinical signs were assessed among the 28 patients with vestibular and/or oculomotor data available.

In the main manuscript, we reported correlations for regions where group differences were observed as part of the primary hypothesis. In addition to these, correlations were also observed in regions where there were trends of group difference in volume. Volume changes in superior occipital gyrus with DEM, left and right pallidum and the posterior limb of the internal capsule with NPC. Several additional regions in the brain correlated with the scores: NPC with anterior insula, cuneus, putamen and posterior limb of the internal capsule, PFV with post central gyrus and the sub-callosal area, and SOT with anterior insula, cuneus and temporal pole. The full-brain GM correlated with SOT. It may be noted that these correlations do not survive multiple comparisons correction. The complete list of regions and their correlations can be found in eTable 6 (β coefficients are reported in mm^3/unit score). The regions reported in eTable 6 are all regions that showed significant correlations ($p < 0.05$).

In the tissue integrity measures, correlations were observed in several regions that demonstrated differences between patients and controls (as part of the primary hypothesis about differences in the cerebellum and the secondary hypothesis about differences in the cerebrum). Changes in FA and MD in some of these regions correlated with the direction of deficit as demonstrated by the scores. Several additional regions showed correlations, without a group difference. List of regions and their corresponding correlations can be found in eTable 7.

As has been explained in the methods in the main manuscript, Mann-Whitney U test was used to assess group differences between patients and controls. Sex and age were nuisance variables which were regressed out before a Mann-Whitney U test was performed on the residuals of the model. In the voxel-wise regression analysis of DTI measures, age and sex effects were observed. eFigure 20 shows various slices where the effects of age and sex on FA and MD maps can be seen. It may be noted that no statistical thresholding was used and thus these effects cannot be considered statistically significant.

Demographics of Patients with Directional Phenomena Exposure Report[a]			
	Men (n=16)	Women (n=14)	Total (N=30)
Age, mean (SD), y	37.38 (8.16)	44.43 (10.55)	40.67 (9.86)
Time from exposure to evaluation, mean (SD), d	214.63 (112.00)	164.43 (107.33)	191.20 (110.91)
[a] Directional phenomena exposure included experiences of sound, pressure, or vibration. Details are in eTable2.			

eTable 1: Demographics of patients with exposure report

	Exposure Report								Clinical Manifestations				
	Associated Sound			Associated Sensory Stimuli					Acute phase		Duration > 3 months		
Case	Sound	High Pitch	Low Pitch	Sensory stimuli	Pressure	Vibration	Movement Attenuation[a]	Time from Exposure to Imaging, d	Acute Symptoms	Subacute Symptoms	Persistent Symptoms	Objective Findings	Required Treatment
1*	X	X					X	91	X	X	X	X	X
2*	X	X					X	187	X	X	X	X	X
3*	X	X					X	286	X	X			
4*	X		X	X		X		4	X	X	X	X	X
5*	X	X		X	X			261	X	X	X	X	X
6*	X		X	X	X		X	235	X	X	X	X	X
7*				X	X		X	181	X	X	X		
8*	X	X					X	147	X	X	X	X	X
9*	X	X		X		X		307	X	X	X	X	X
10*	X	X		X	X			332	X	X	X	X	X
11*	X	X		X	X			300	X	X	X	X	X
12*	X	X					X	284	X	X	X	X	X
13*	X	X					X	284	X	X	X	X	X
14*	X	X		X	X		X	22	X	X	X	X	X
15*	X	X					X	250	X	X	X	X	X
16*	X	X		X	X		X	234	X	X	X	X	X
17*									X	X	X	X	X
18*	X	X		X	X			300	X	X	X		
19*				X	X		X	159	X	X	X	X	X
20*	X	X						189	X	X	X	X	X
21	X	X						?		X	X	X	X
22										X	X	X	LTF
23													
24				X	X		X	196	X	X	X	X	LTF
25				X	X			53	X	X	X	X	X
26	X	X						27					
27										X	X	X	X
28													
29	X	X		X	X		X	11	X	X	LTF	LTF	LTF
30	X		X	X		X	X	51	X	X	LTF	LTF	LTF
31	X	X						?		X	X	X	X
32										X	X	X	X
33										X	X	X	
34	X	X						?					
35				X	X		X	?	X	X			
36													
37											X	X	
38	X	X						403	X	X	X	X	
39	X	X					X	144		X	X	X	
40													

[a] Patients reported attenuation of sound, pressure or vibration when moving to a different location
* Was a participant in [68]
? Could not provide an exact date of their directional phenomena exposure report
LTF Lost to follow-up
Individuals above without a defined exposure report listed were referred to the University of Pennsylvania by the US Department of State for clinical evaluation and treatment for a possible uncharacterized directional phenomena exposure even though they didn't have a clearly defined exposure report, for example in instances such as family members of USG personnel with defined exposure reports. Additional information cannot be provided due to privacy and National Security concerns.

eTable 2: Exposure descriptions of the directional phenomena

Case	Sensory Organization Test (SOT)	Developmental Eye Movements test (DEM)	Near Point Convergence (NPC)	Positive Fusional Vergence (PFV)
1*	41	29	7.5	35
2*	78	25	2.5	25
3*				
4*	71	32	2.5	25
5*	59	40	13	12
6*	78	27	10	30
7*				
8*	45			
9*	43	53	12	20
10*	52	58	7.5	16
11*	68			
12*	48	40	10	18
13*		50	5	30
14*	61	40	13	6
15*	14	74	7.5	30
16*	26	67	25	18
17*	45	38	5	18
18*				
19*	20	90	7.5	6
20*	56	37	7.5	25
21	79	34	5	35
22	82			
23				
24				
25	78			
26				
27		39	10	18
28				
29	43	39	5	16
30				
31	66	30.4	2.5	40
32	77			
33	73	26.8	5	40
34				
35				
36				
37	84			
38	74			
39	81			
40				
Total (Male)	26 (15)	20 (10)	20 (10)	20 (10)
* Was a participant in [68]				

eTable 3: Distribution of clinical scores (measures of clinical assessment) used for correlation with imaging. These scores serve as measures of vestibular and oculomotor function and were obtained as part of the clinical evaluation and are used to investigate potential correlation with imaging. The Sensory Organization Test (SOT) [72] (range 14-84, >=70 indicates normal) measures vestibular function, and evaluates postural control and postural sway using computerized dynamic posturography. The assessment of oculomotor functions included two measures of vergence [73, 74], near point of convergence (NPC) (range 2.5-25cm, <=6cm indicates normal) and positive fusional vergence (PFV) (range 6-40 prism diopters base-out, >=20 prism diopters base-out indicates normal), as well as a measure of saccadic eye movement, the Developmental Eye Movement test (DEM) [75] (range 25-90 seconds, <= 30 seconds indicates normal).

Visuospatial / “Intraparietal Sulcus – Frontal Eye Fields” Network

Region Names	Brodmann Areas	Alternative Name
Left Middle Frontal Gyrus, Superior Frontal Gyrus, Precentral Gyrus	6	Supplemental Eye Field Left
Left Inferior Parietal Sulcus	2, 40, 7	Intraparietal Sulcus Left
Left Frontal Operculum, Inferior Frontal Gyrus	44, 48, 45	Frontal Eye Field Left
Left Inferior Temporal Gyrus	37	Inferior Temporal Gyrus Left
Right Middle Frontal Gyrus	6	Middle Frontal Right
Right Inferior Parietal Lobule	2, 40, 7	Intraparietal Sulcus Right
Right Frontal Operculum, Inferior Frontal Gyrus	44, 48	Frontal Eye Field Right
Right Middle Temporal Gyrus	37	Inferior Temporal Right
Left Lobule VIII, Lobule VIIb	N/A	Lobule VIII, Lobule VIIb Left
Right Lobule VIII, Lobule VIIb	N/A	Lobule VIII, Lobule VIIb Right
Right Lobule VI, Crus I	N/A	Lobule VI, Crus I Right

Auditory Network

Region Names	Brodmann Areas	Alternative Name
Left Superior Temporal Gyrus, Heschl’s Gyrus	22, 48	Superior Temporal Gyrus Left
Right Superior Temporal Gyrus	22, 38, 42, 48	Superior Temporal Gyrus Right
Right Thalamus	N/A	Thalamus Right

eTable 4: Regions involved in the visuospatial and auditory networks as reported in [60].

Region	DTI Scalar	U	rank-biserial correlation	p-value	FDR q
Left Cerebellum - Somatomotor	MD	1012	-0.307	0.019	0.033
Left Cerebellum - Dorsal Attention	MD	1275	-0.647	8.36x10-7	1.34x10-5
Left Cerebellum - Ventral Attention	MD	921	-0.19	0.149	0.149
Left Cerebellum - Limbic	MD	1185	-0.531	5.33x10-5	0.000426
Left Cerebellum - Frontoparietal	MD	991	-0.28	0.033	4.26x10-4
Left Cerebellum - Default	MD	1150	-0.486	2.19x10-4	0.001
Right Cerebellum - Somatomotor	MD	1025	-0.324	0.014	0.027
Right Cerebellum - Dorsal Attention	MD	1104	-0.426	0.001	0.004
Right Cerebellum - Ventral Attention	MD	932	-0.204	0.121	0.121
Right Cerebellum - Limbic	MD	1106	-0.429	0.001	0.004
Right Cerebellum - Frontoparietal	MD	942	-0.217	0.099	0.099
Right Cerebellum - Default	MD	1020	-0.318	0.016	0.031
Left Cerebellar WM	MD	870	-0.124	0.347	0.347
Right Cerebellar WM	MD	916	-0.183	0.164	0.164
Left Cerebellar WM	FA	624	0.194	0.141	0.141
Right Cerebellar WM	FA	665	0.141	0.285	0.286

eTable 5: Functionally defined regions of cerebellum that showed differences in MD and FA.

Abbreviations: DTI, Diffusion tensor imaging; FDR, false discovery rate; MD, mean diffusivity; WM, white matter

Score	Region	Hemi-sphere	Tissue type	β (Score)	95% CI (Score)	p-value (Score)	Adjus-ted R^2	β (Group Difference)	95% CI (Group Difference)	p-value (Group Difference)	FDR p-value (Group Difference)
DEM	middle temporal gyrus*	R	GM	36.42	4.32, 68.53	0.029	0.66	-639.73	-1205.54, -73.93	0.027	0.11
DEM	superior occipital gyrus*	L	GM	13.20	2.90, 23.51	0.015	0.34	237.00	24.41, 449.58	0.029	0.12
NPC	pallidum*	R	GM	24.21	13.13, 35.28	0.000	0.74	55.18	2.17, 108.19	0.042	0.12
NPC	pallidum*	L	GM	23.06	9.14, 36.97	0.003	0.69	71.84	16.63, 127.04	0.011	0.057
NPC	putamen	R	GM	61.36	12.66, 110.06	0.017	0.65	-67.64	-230.31, 95.04	0.41	0.41
NPC	putamen	L	GM	63.45	19.71, 107.18	0.007	0.69	-95.13	-251.87, 61.61	0.23	0.25
NPC	ventral DC**	R	WM	34.48	0.24, 68.72	0.049	0.72	201.64	80.59, 322.69	0.001	0.011
NPC	ventral DC**	L	WM	37.40	2.07, 72.72	0.039	0.72	205.59	66.67, 344.50	0.004	0.029
NPC	posterior limb of internal capsule*	R	WM	18.70	1.30, 36.09	0.037	0.72	-90.04	-172.17, -7.92	0.032	0.12
NPC	anterior insula	R	GM	60.08	28.01, 92.16	0.001	0.81	-47.72	-197.69, 102.24	0.53	0.53
NPC	anterior insula	L	GM	67.00	26.19, 107.80	0.003	0.73	7.49	-150.92, 165.90	0.93	0.93
NPC	cuneus	R	GM	76.77	1.59, 151.96	0.046	0.56	-69.27	-400.21, 261.68	0.68	0.68
NPC	parietal operculum	R	GM	35.56	3.78, 67.35	0.031	0.43	-80.98	-234.21, 72.25	0.30	0.30
NPC	triangular part of inferior frontal gyrus	R	GM	60.95	9.96, 111.93	0.022	0.49	25.92	-192.79, 244.63	0.81	0.81
PFV	angular gyrus	L	GM	-58.47	-116.16, -0.77	0.047	0.49	-537.03	-1157.53, 83.46	0.089	0.21
PFV	frontal pole	R	GM	-17.84	-35.49, -0.18	0.048	0.57	171.81	-15.01, 358.63	0.071	0.21
PFV	postcentral gyrus	R	GM	-56.87	-106.65, -7.08	0.028	0.50	-27.48	-492.09, 437.13	0.91	0.91
PFV	subcallosal area*	R	GM	-15.16	-25.91, -4.40	0.009	0.56	-99.82	-193.06, -6.59	0.036	0.12
PFV	subcallosal area	L	GM	-16.24	-28.71, -3.77	0.014	0.50	-40.87	-145.42, 63.67	0.44	0.44
SOT	anterior insula	L	GM	-11.49	-21.81, -1.18	0.031	0.45	7.49	-150.92, 165.90	0.93	0.93
SOT	cuneus	R	GM	-16.56	-33.00, -0.12	0.048	0.33	-69.27	-400.21, 261.68	0.68	0.68
SOT	precunues	L	GM	-38.26	-71.94, -4.57	0.028	0.55	531.75	-91.51, 1155.01	0.093	0.21
SOT	supramarginal gyrus	L	GM	-21.51	-42.82, -0.20	0.048	0.51	-183.39	-633.30, 266.51	0.42	0.42
SOT	temporal pole	L	GM	-32.80	-56.84, -8.75	0.010	0.66	339.14	-103.61, 781.89	0.13	0.25
SOT	All GM	B	GM	-464.47	-924.24, -4.70	0.048	0.91	6720.44	-4829.52, 18270.40	0.25	0.25
** Region volume is significantly different between patients and controls using FDR											
* Region volume difference between patients and controls is a trend with uncorrected p-value < 0.05											

eTable 6: Regions that show correlations with imaging-based volume measurements

Abbreviations: CI, Confidence Interval; WM, white matter; GM, grey matter; FDR, False Discovery Rate; L, Left; R, Right; SOT, Sensory Organization Test; DEM, Developmental Eye Movement test: NPC, Near Point Convergence; PFV, Positive Fusional Vergence

Legend: These are the regions that show trends of correlations with the imaging-based volume measurements. 139 regions of the Muse Atlas [65] along with two regions for all WM and all GM, totaling 141 regions, were tested, for 4 scores. β coefficients are interpreted as mm^3 per unit of clinical score. For detailed explanation of the clinical scores, their ranges and anchor values, please see legend of eTable 3. Only those regions that demonstrate trends of significance are presented in the table.

Scalar	Score	Region	Hemi-sphere	Tissue type	β (Score)	95% CI (Score)	p-value (Score)	Adjusted R^2	β (Group Difference)	95% CI (Group Difference)	p-value (Group Difference)
FA	DEM	pons	R	Bstem	-5.19E-4	-9.19E-4, -1.19E-4	0.014	0.48	-6.20E-3	-1.57E-2, 3.32E-3	0.20
FA	DEM	fornix/stria terminalis	L	WM	5.64E-4	3.14E-5, 1.10E-3	0.039	0.15	4.80E-3	-3.56E-3, 1.32E-2	0.26
FA	DEM	fornix	R	WM	8.76E-4	4.44E-5, 1.71E-3	0.040	0.15	-8.46E-3	-2.44E-2, 7.47E-3	0.29
FA	DEM	superior fronto-occipital fasciculus	L	WM	1.04E-3	8.15E-6, 2.07E-3	0.048	0.20	3.87E-3	-9.73E-3, 1.75E-2	0.57
FA	NPC	rectus wm	L	WM	4.24E-3	9.07E-5, 8.40E-3	0.046	0.12	1.06E-2	-1.36E-3, 2.26E-2	0.082
FA	NPC	superior temporal wm	R	WM	-1.64E-3	-3.26E-3, -7.16E-6	0.049	0.32	-5.93E-4	-8.67E-3, 7.49E-3	0.88
FA	PFV	middle fronto-orbital wm	R	WM	-2.39E-3	-3.81E-3, -9.72E-4	0.0027	0.43	-1.74E-2	-3.10E-2, -3.77E-3	0.013
FA	PFV	cerebellum	R	Cere GM	-6.50E-4	-1.22E-3, -8.31E-5	0.027	0.18	6.84E-3	1.22E-3, 1.25E-2	0.018
FA	PFV	superior cerebellar peduncle	R	Cere WM	-1.12E-3	-2.04E-3, -1.95E-4	0.021	0.43	-6.58E-3	-1.54E-2, 2.25E-3	0.14
FA	PFV	middle fronto-orbital wm	L	WM	-1.99E-3	-3.95E-3, -3.10E-5	0.047	0.21	-7.90E-3	-2.12E-2, 5.38E-3	0.24
FA	PFV	inferior cerebellar peduncle	L	Cere WM	-1.46E-3	-2.40E-3, -5.14E-4	0.005	0.40	5.59E-3	-4.79E-3, 1.60E-2	0.29
FA	PFV	superior fronto-occipital fasciculus	R	WM	-2.15E-3	-4.16E-3, -1.49E-4	0.037	0.27	4.27E-3	-8.21E-3, 1.68E-2	0.50
FA	PFV	inferior cerebellar peduncle	R	Cere WM	-1.79E-3	-3.11E-3, -4.61E-4	0.012	0.33	4.45E-4	-1.13E-2, 1.22E-2	0.94
FA	SOT	substancia nigra	R	Subctx	1.66E-3	1.62E-4, 3.15E-3	0.032	0.10	-1.40E-2	-3.53E-2, 7.34E-3	0.20
FA	SOT	postcentral wm	R	WM	6.82E-4	1.33E-5, 1.35E-3	0.046	0.07	-4.55E-3	-1.56E-2, 6.47E-3	0.41
FA	SOT	cuneus wm	L	WM	1.20E-3	3.71E-4, 2.02E-3	0.0067	0.39	1.01E-3	-1.32E-2, 1.52E-2	0.89
FA	SOT	precentral wm	R	WM	5.20E-4	5.02E-5, 9.91E-4	0.032	0.11	4.80E-4	-8.66E-3, 9.62E-3	0.92
FA	SOT	middle cerebellar peduncle	L	Cere WM	9.01E-4	9.59E-5, 1.71E-3	0.030	0.27	4.66E-5	-1.40E-2, 1.41E-2	0.99
MD	DEM	cerebellum wm	R	Cere WM	-4.60E-7	-9.01E-7, -1.87E-8	0.042	0.39	-8.97E-6	-2.12E-5, 3.31E-6	0.15
MD	DEM	hippocampus	L	GM	-1.58E-6	-3.09E-6, -7.58E-8	0.041	0.23	6.90E-6	-1.02E-5, 2.40E-5	0.42
MD	DEM	fornix	L	WM	-7.71E-6	-1.54E-5, -6.18E-9	0.050	0.11	1.26E-5	-4.13E-5, 6.63E-5	0.64
MD	DEM	uncinate fasciculus	L	WM	3.53E-6	1.24E-6, 5.82E-6	0.005	0.31	-4.27E-6	-2.92E-5, 2.07E-5	0.73
MD	DEM	uncinate fasciculus	R	WM	2.28E-6	4.76E-7, 4.08E-6	0.017	0.21	-6.73E-7	-2.93E-5, 2.80E-5	0.96
MD	NPC	inferior occipital wm	L	WM	3.01E-6	7.40E-7, 5.28E-6	0.013	0.59	-6.50E-6	-1.72E-5, 4.20E-6	0.23
MD	NPC	fusiform wm	R	WM	2.11E-6	1.04E-7, 4.11E-6	0.041	0.52	3.93E-6	-6.30E-6, 1.42E-5	0.44
MD	NPC	postcentral wm	R	WM	4.76E-6	1.64E-7, 9.35E-6	0.043	0.10	4.97E-6	-1.18E-5, 2.18E-5	0.56
MD	PFV	middle frontal gyrus	R	GM	7.76E-6	7.44E-7, 1.48E-5	0.032	0.37	3.47E-5	5.80E-6, 6.37E-5	0.019
MD	PFV	inferior frontal gyrus	L	GM	6.76E-6	1.81E-6, 1.17E-5	0.011	0.31	2.42E-5	2.34E-6, 4.60E-5	0.031
MD	PFV	inferior cerebellar peduncle	L	Cere WM	4.36E-6	2.18E-7, 8.50E-6	0.040	0.13	-2.85E-5	-6.73E-5, 1.01E-5	0.15
MD	PFV	insula	R	GM	3.36E-6	4.90E-7, 6.23E-6	0.025	0.24	5.33E-6	-9.60E-6, 2.03E-5	0.48
MD	PFV	gyrus rectus	R	GM	4.62E-6	1.64E-6, 7.61E-6	0.0048	0.31	6.67E-6	-1.21E-5, 2.54E-5	0.48
MD	PFV	middle fronto-orbital gyrus	R	GM	4.40E-6	2.01E-6, 6.79E-6	0.0014	0.46	6.23E-6	-1.64E-5, 2.88E-5	0.58
MD	PFV	middle cerebellar peduncle	L	Cere WM	9.21E-6	1.54E-7, 1.83E-5	0.047	0.23	1.23E-5	-4.43E-5, 6.87E-5	0.67
MD	PFV	uncinate fasciculus	L	WM	-5.89E-6	-1.07E-5, -1.04E-6	0.021	0.18	-4.27E-6	-2.92E-5, 2.07E-5	0.73
MD	PFV	insula	L	GM	5.90E-6	1.63E-6, 1.02E-5	0.010	0.37	2.38E-6	-1.41E-5, 1.88E-5	0.77
MD	PFV	middle cerebellar peduncle	R	Cere WM	1.25E-5	2.73E-6, 2.22E-5	0.015	0.37	-2.52E-6	-6.40E-5, 5.90E-5	0.94
MD	PFV	uncinate fasciculus	R	WM	-5.00E-6	-8.25E-6, -1.76E-6	0.0050	0.31	-6.73E-7	-2.93E-5, 2.80E-5	0.96
MD	SOT	cerebellum	R	Cere GM	1.65E-6	1.22E-7, 3.17E-6	0.036	0.17	-3.53E-5	-6.37E-5, -6.80E-6	0.016
MD	SOT	middle occipital wm	L	WM	-5.28E-7	-8.33E-7, -2.23E-7	0.0018	0.58	-8.50E-6	-1.86E-5, 1.67E-6	0.10
MD	SOT	superior cerebellar peduncle	R	Cere WM	1.42E-6	1.02E-7, 2.75E-6	0.036	0.11	-1.25E-5	-3.18E-5, 6.70E-6	0.20
MD	SOT	medial lemniscus	R	Bstem	9.65E-7	2.78E-8, 1.90E-6	0.044	0.08	-7.63E-6	-2.68E-5, 1.16E-5	0.43
MD	SOT	postcentral wm	R	WM	-8.14E-7	-1.57E-6, -5.36E-8	0.037	0.15	4.97E-6	-1.18E-5, 2.18E-5	0.56
MD	SOT	substancia nigra	R	Subctx	-2.05E-6	-3.81E-6, -2.81E-7	0.025	0.13	-4.53E-6	-2.16E-5, 1.25E-5	0.60

eTable 7: Regions showing correlations with imaging-based tissue integrity measurements
Abbreviations: CI, Confidence Interval; WM, white matter; GM, grey matter; FDR, False Discovery Rate; L, Left; R, Right; SOT, Sensory Organization Test; DEM, Developmental Eye Movement test: NPC, Near Point Convergence; PFV, Positive Fusional Vergence; FA, Fractional Anisotropy; MD, Mean Diffusivity; Cere, Cerebellum
Legend: 176 regions of the JHU Atlas [67] were tested were tested for correlation with 4 scores, and 4 diffusion indices. Only those that demonstrate trends of significance are presented in the table. β (score) coefficients are in unit of diffusion index measure (mm^2/s for MD, unitless for FA) per unit of clinical score. β (group) coefficients are in unit of diffusion index per unit of clinical score.

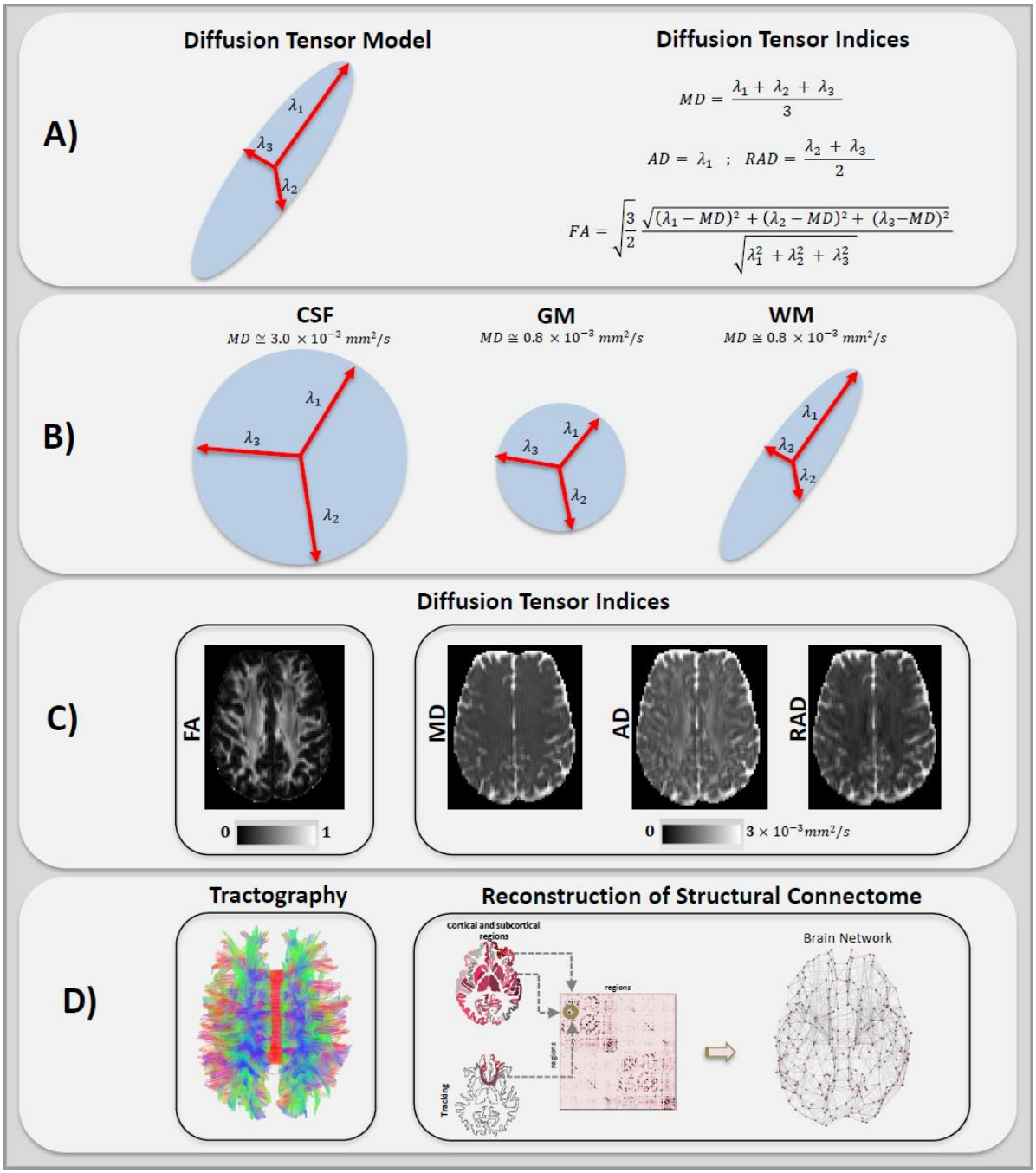

eFigure 1: Details of Diffusion Tensor Imaging (DTI) – acquisition, indices, tractography and creation of the connectome.

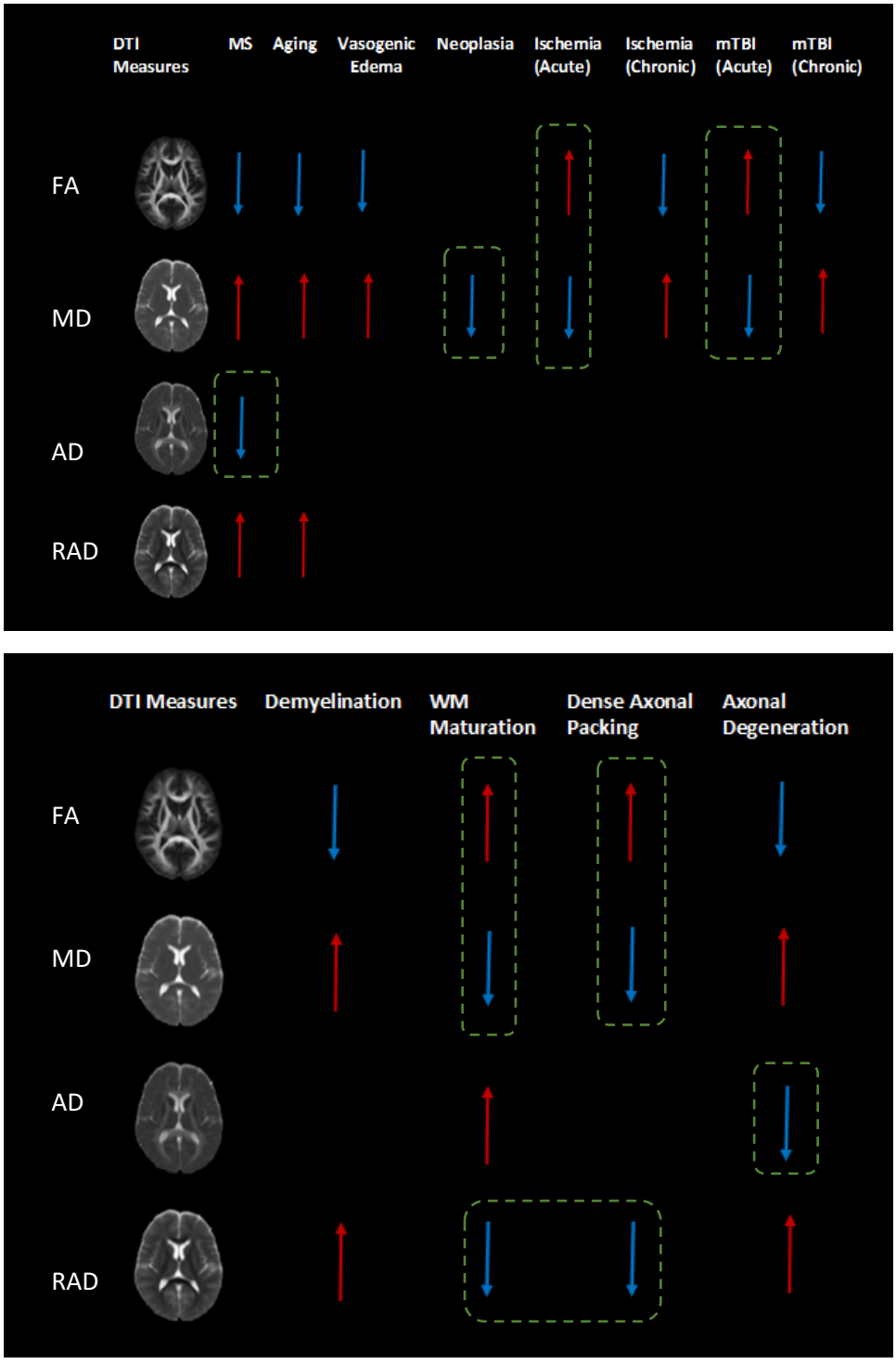

eFigure 2: Patterns of variation in tissue microstructural integrity measures of fractional anisotropy (FA), mean diffusivity (MD), axial diffusivity (AD) and radial diffusivity (RAD) reported in various pathologies (top) and seen in various mechanisms (bottom). Red upward arrow indicates an increase, and a blue downward arrow indicates a decrease in that measure. The green boxes highlight the direction of differences observed in the patients.

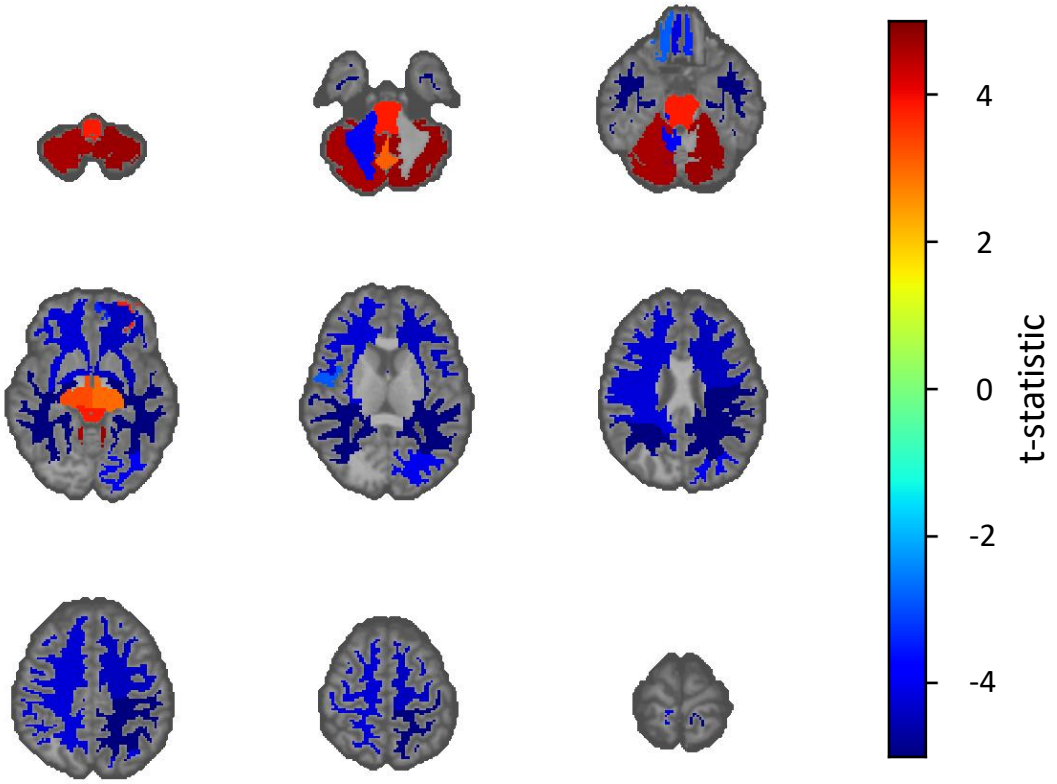

eFigure 3: FDR-corrected group differences on region volumes of the MUSE atlas. Regions which survive FDR correction are displayed on a series of axial slices of the brain, color coded by t-statistic. White matter structures throughout the brain were found to have lower volume in the patient group. Cerebellar gray matter and brain stem structures were found to have higher volume in patients.

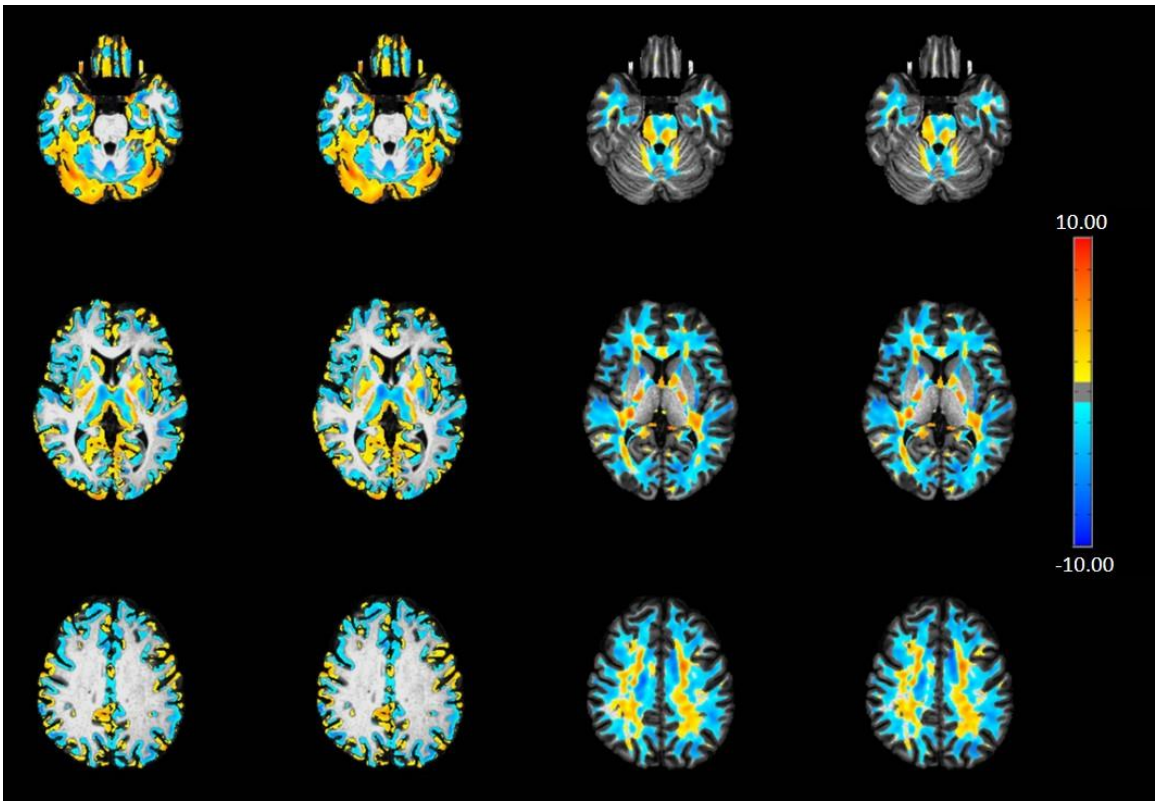

eFigure 4: Volumetric analysis repeated by excluding the PBI cohort. In columns from left to right: GM effect sizes (rank-biserial correlation) of the Mann-Whitney U tests of the full patients versus controls; GM effect sizes of the patients without the PBI subgroup versus controls; WM effect sizes of the full patients versus controls; and WM effect sizes of the patients without the PBI subgroup versus controls. Effect sizes are displayed regardless of statistical significance.

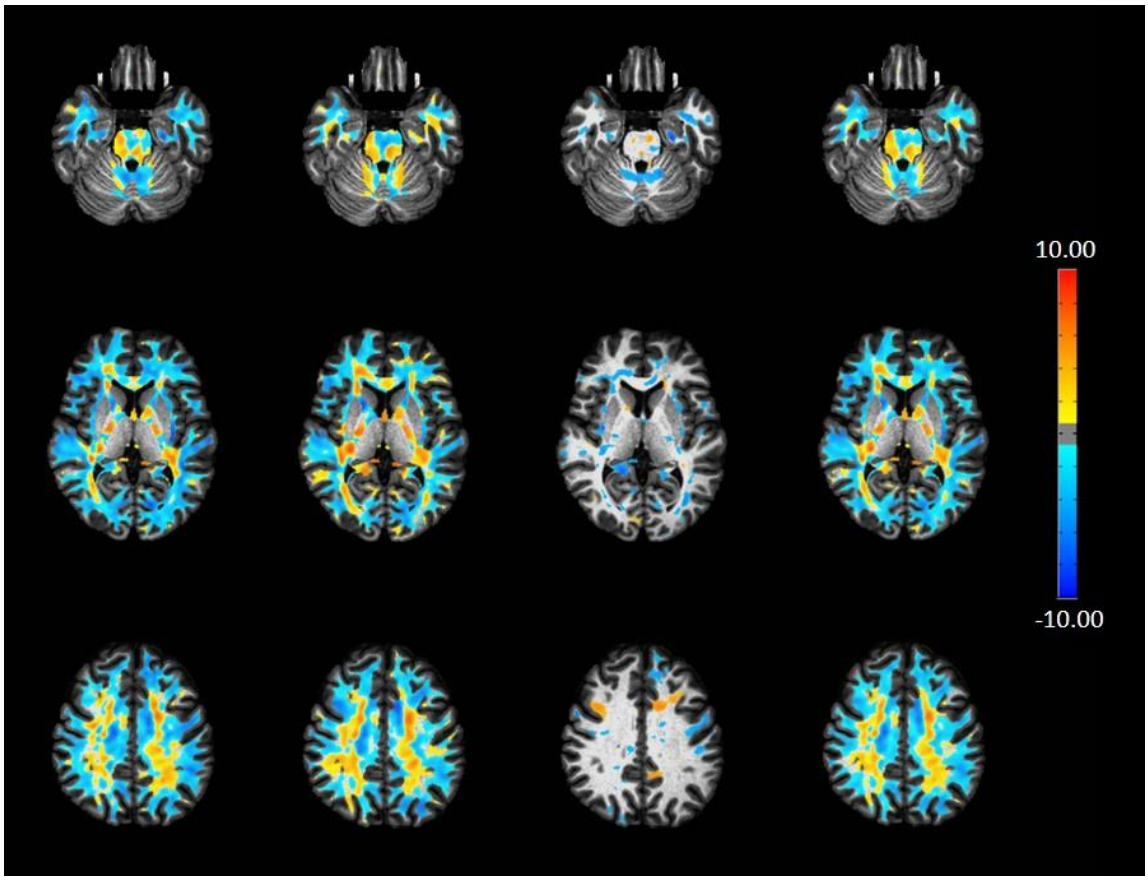

eFigure 5: Replication of WM volumetric analysis in comparison to different control cohorts. In columns from left to right effect sizes of the Mann-Whitney U test (statistically unthresholded): (column 1) patients vs control set 1; (column 2) patients vs control set 2; (column 3) control set 1 vs control set 2, $p < 0.05$, uncorrected; and (column 4) patients vs the combined controls.

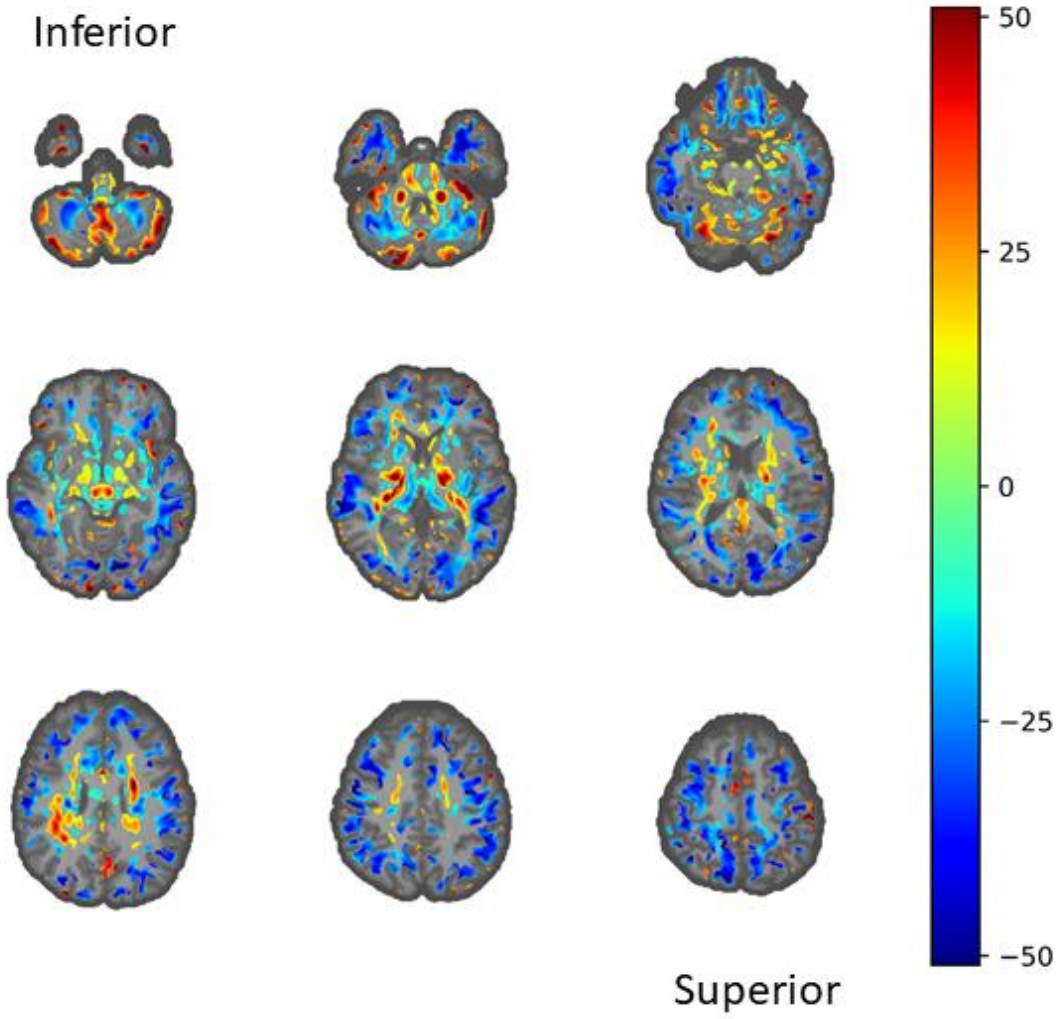

eFigure 6: Percentage volume change in the patients compared to their controls: Axial slices of the template showing percent difference in mean tissue volume between patients and controls, as calculated from RAVENS maps. Slices start from inferior-most in the top left and proceed left-to-right to superior in the bottom right. A linear regression model with terms for group, age, sex, and ICV was fitted and the coefficients for group term and intercept term were collected. Percent difference was calculated as 100 multiplied by the ratio of the group coefficient to the intercept. Positive values indicate higher tissue volume in the patient group; negative values indicate higher local volume in the control groups. The color bar shows values between -50% to +50%, but voxels exist where the percent difference exceeds 50% in magnitude.

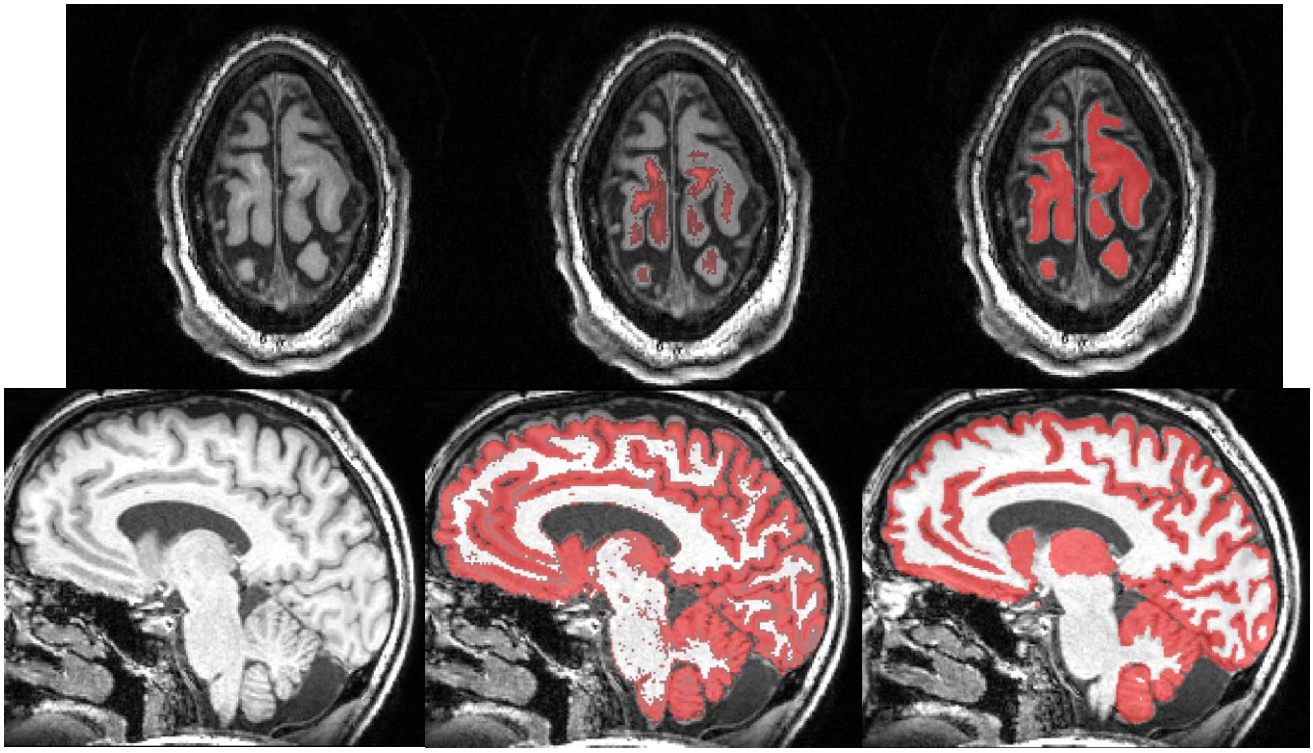

eFigure 7: Comparison of GM segmentation between CAT12 and MUSE: Representative slices from (column 1) original T1 image; (column 2) CAT12's GM tissue probability maps thresholded at 0.05, and shown as red overlays on the T1 slices and (column 3) is the MUSE segmentation of the GM overlaid in red on the T1 map. It is evident that CAT12 under segments the GM in the superior cortical areas, while MUSE's GM mask manages to recover this tissue.

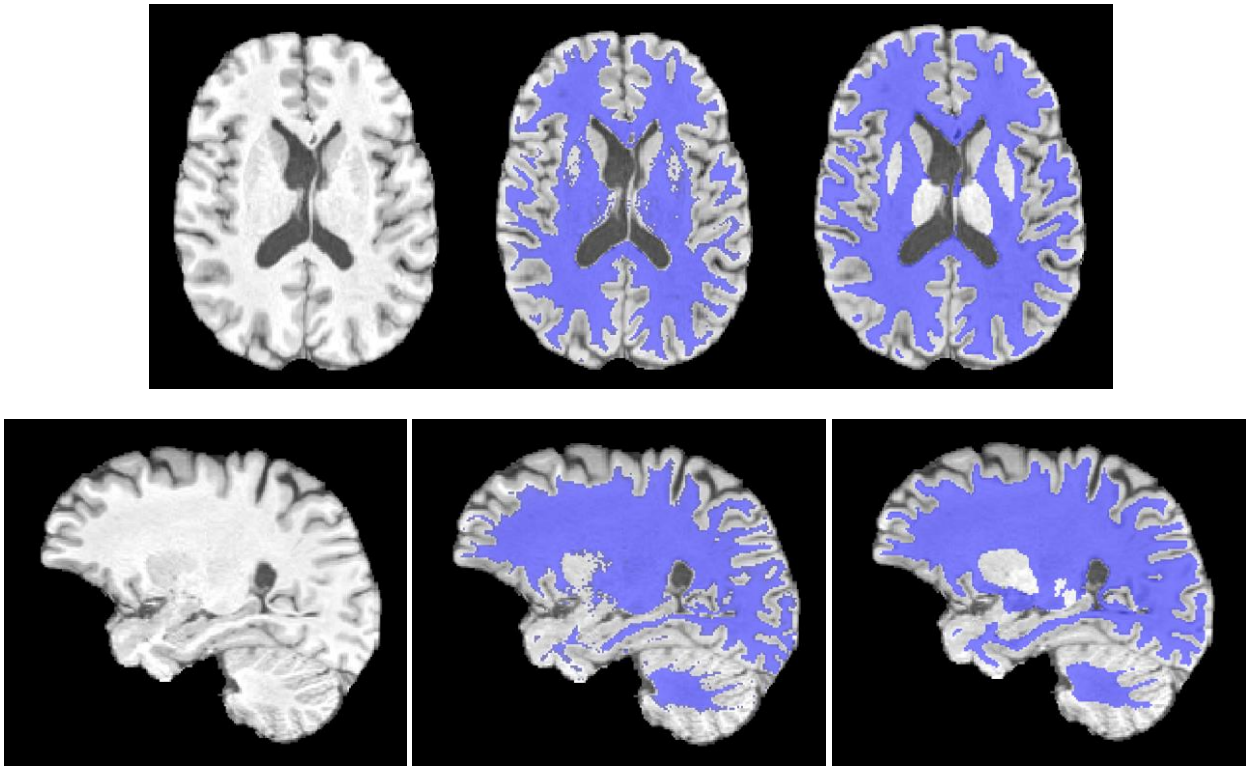

eFigure 8: Comparison of White Matter Segmentation between CAT12 and MUSE: Representative slices from (column 1) original T1 image; (column 2) CAT12's WM tissue probability maps thresholded at 0.05, and shown as blue overlays on the T1 slices and (column 3) is the MUSE segmentation of the WM overlaid in blue on the T1 map. A visual comparison of columns 2 and 3 show that CAT12 under segments the WM in the superior peripheral areas, while MUSE's WM mask manages to recover this tissue. There is also a clear spread of the WM compartment into subcortical gray matter areas in CAT12, while MUSE segmentation respects this tissue boundary.

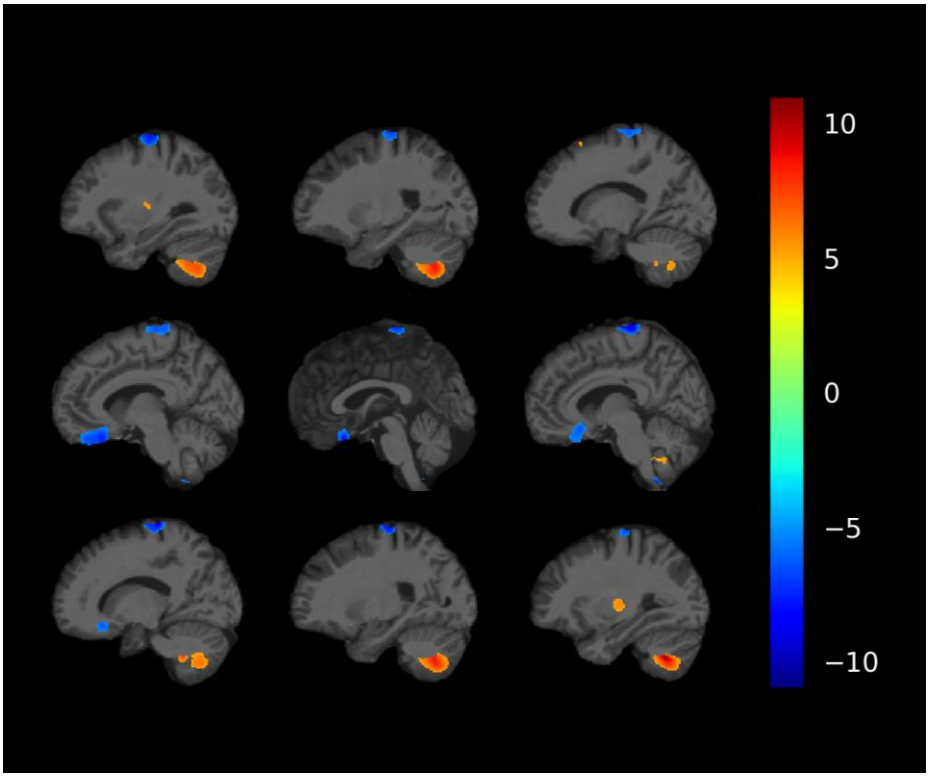

eFigure 9: Results of the SPM-CAT12 pipeline, displayed through sagittal slices. The patients displayed a reduction in GM volume in regions of the inferior frontal lobe, and superior cortical regions, compared to controls. Additionally, an increased volume was noticed in the deep cerebellar gray matter. T-statistics results are displayed after clusterizing at 100 voxels and controlling for family-wise error rate (FWER 0.05). The color bar represents the range of t-statistics.

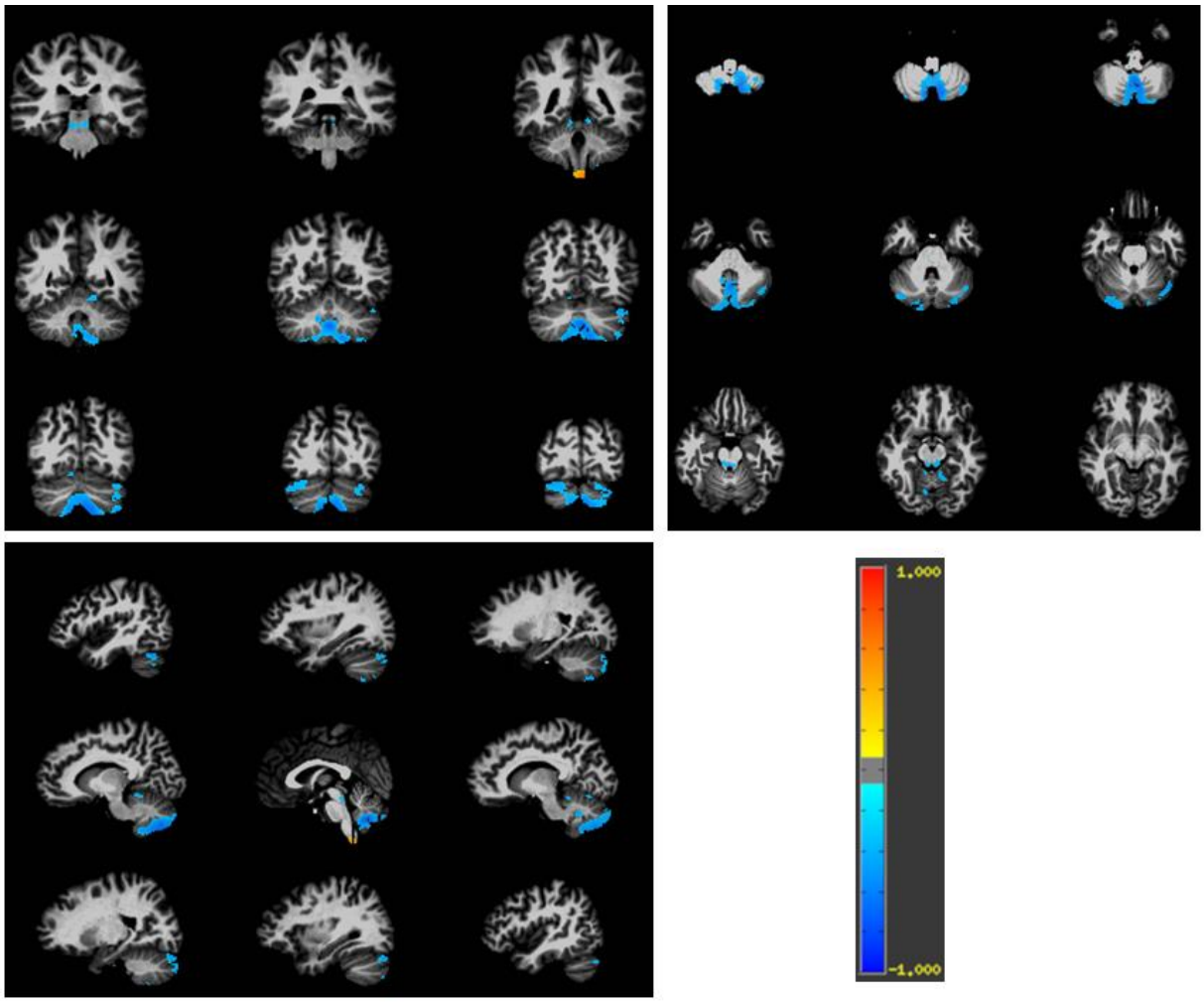

eFigure 10: Representative slices (in coronal, sagittal and axial views) showing significant differences in AD in the cerebellum and regions of the colliculi in patients compared to the controls. The color bar shows the effect size of difference and indicates that the AD values are lower in the patients compared to controls.

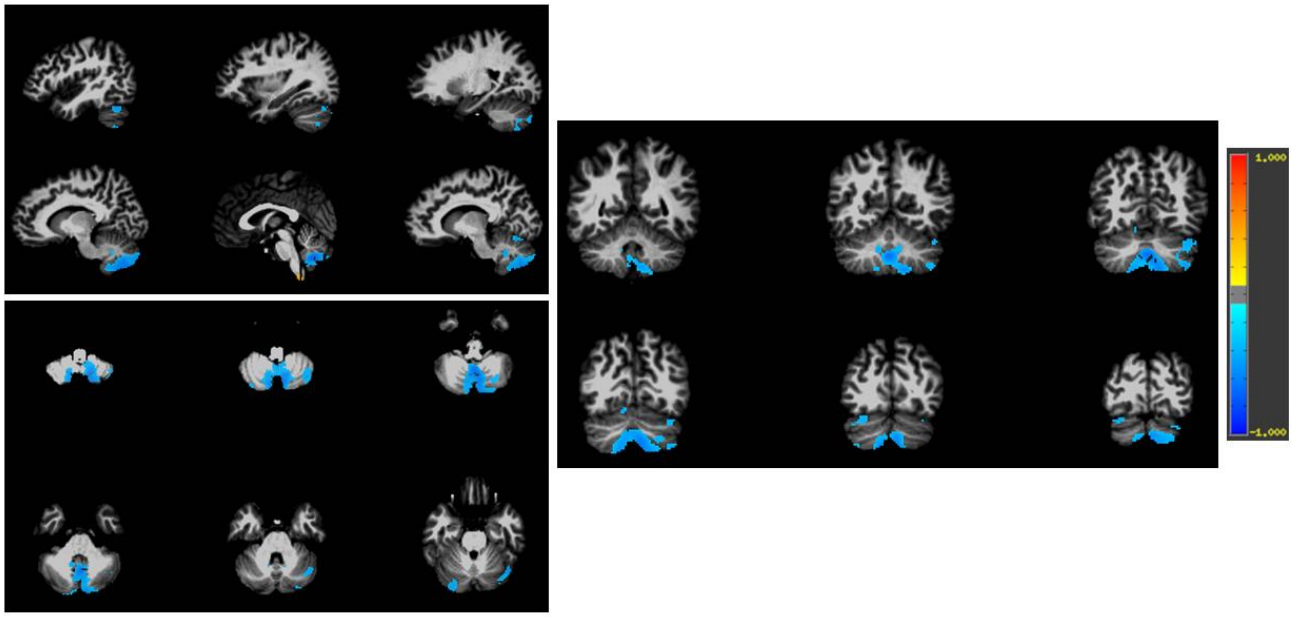

eFigure 11: Representative slices (in coronal, sagittal and axial views) showing significant differences in RAD in the cerebellum of the patients compared to the controls. The color bar shows the effect size of difference and indicates that the RAD values are lower in patients compared to controls.

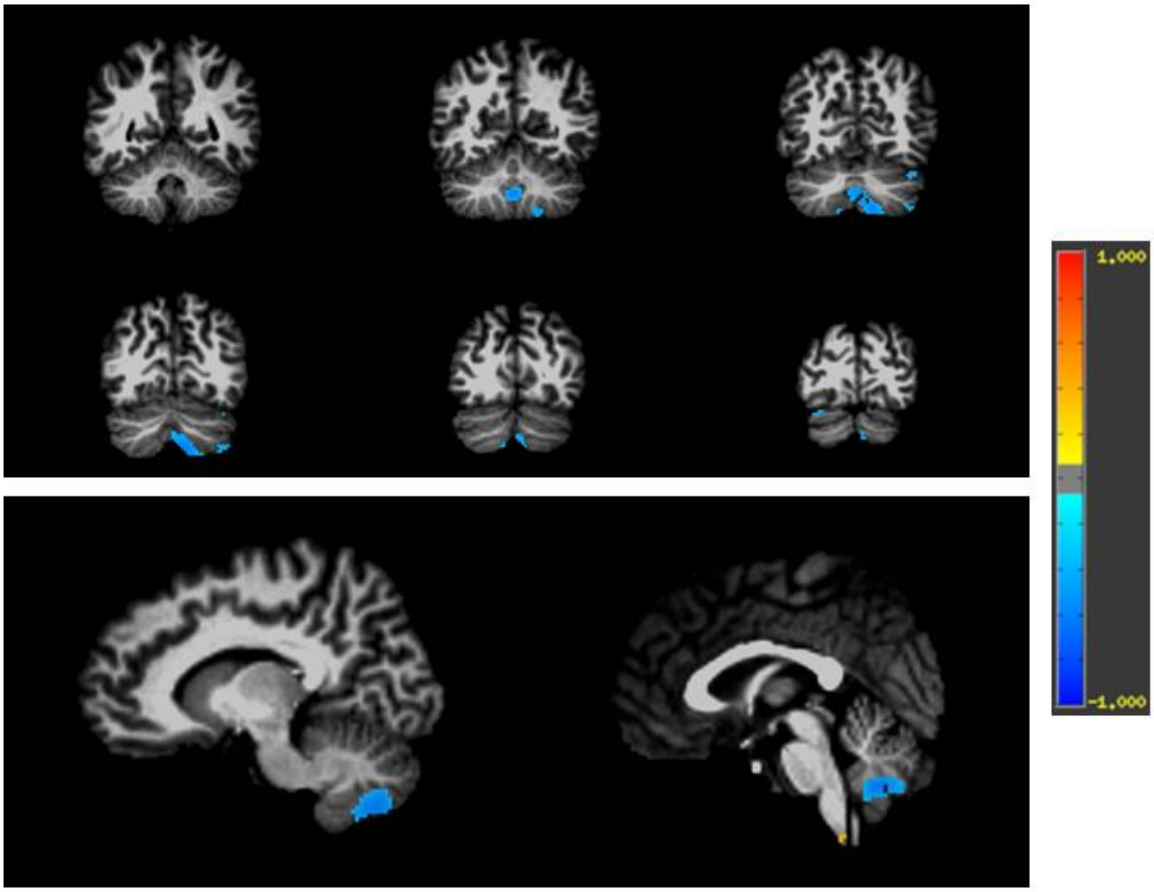

eFigure 12: Representative slices showing significant differences in free water volume fraction (VF) in the cerebellum of the patients compared to the controls. The color bar shows the effect size of difference and indicates that the VF values are lower in patients compared to controls.

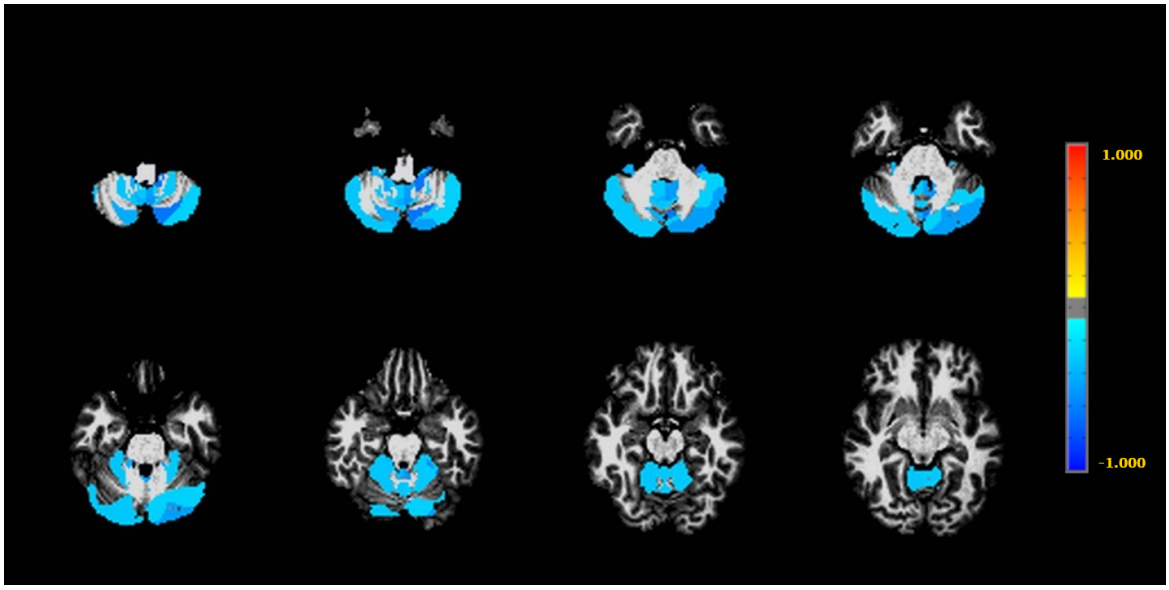

eFigure 13: ROI-based analysis of the MD maps of the cerebellum, parcellated into functionally defined regions. The regions showing significant difference are color-coded with effect size that indicates lower MD in patients as compared to the controls. The region-wise values are available in eTable 5.

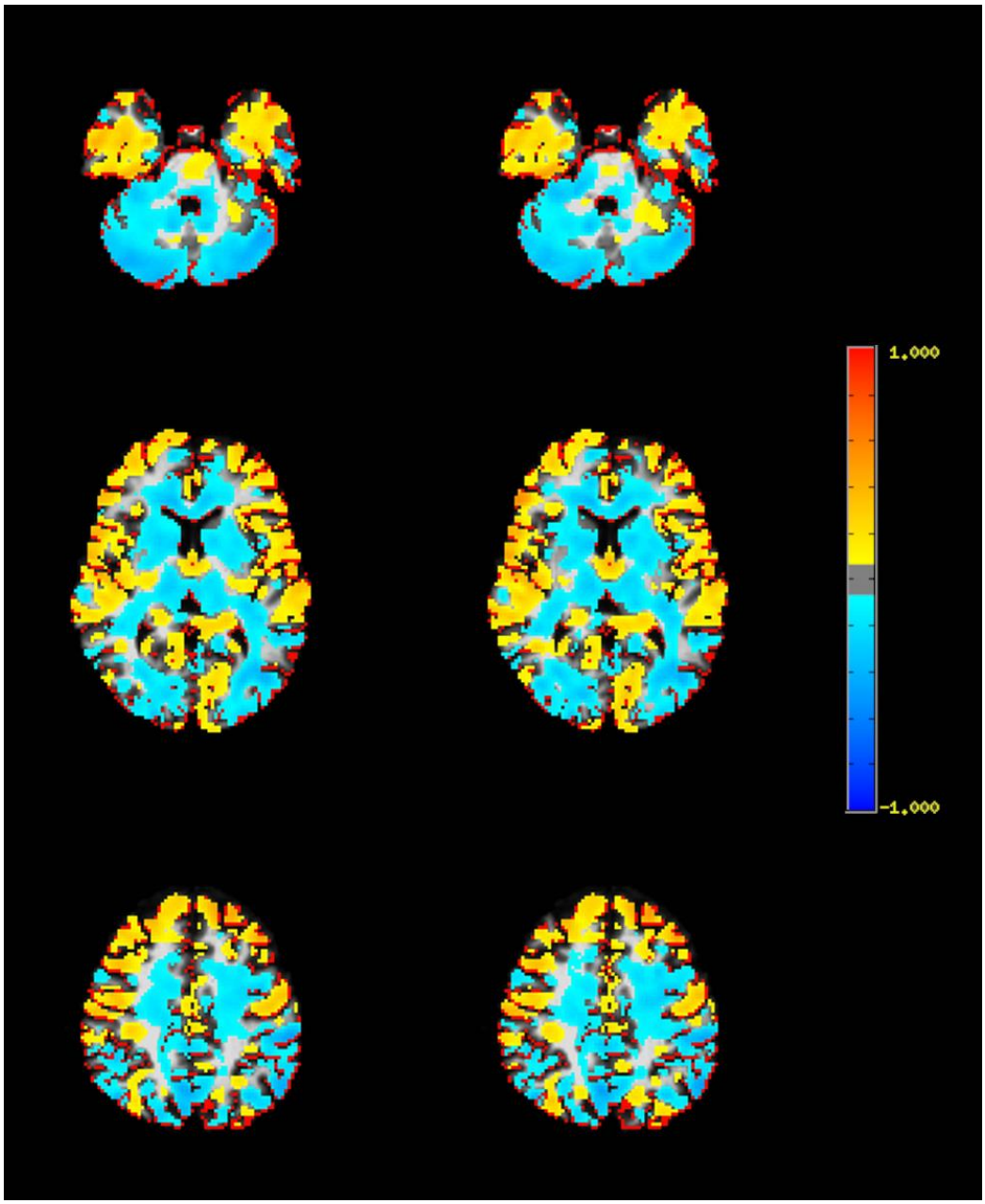

eFigure 14: Tissue integrity analysis by excluding the PBI cohort. (Left) effect sizes (rank-biserial correlation) of the Mann-Whitney U test on Mean Diffusivity of the full patients versus controls, and (Right) effect sizes of the patients without the PBI subgroup versus controls. Effect sizes are displayed regardless of statistical significance.

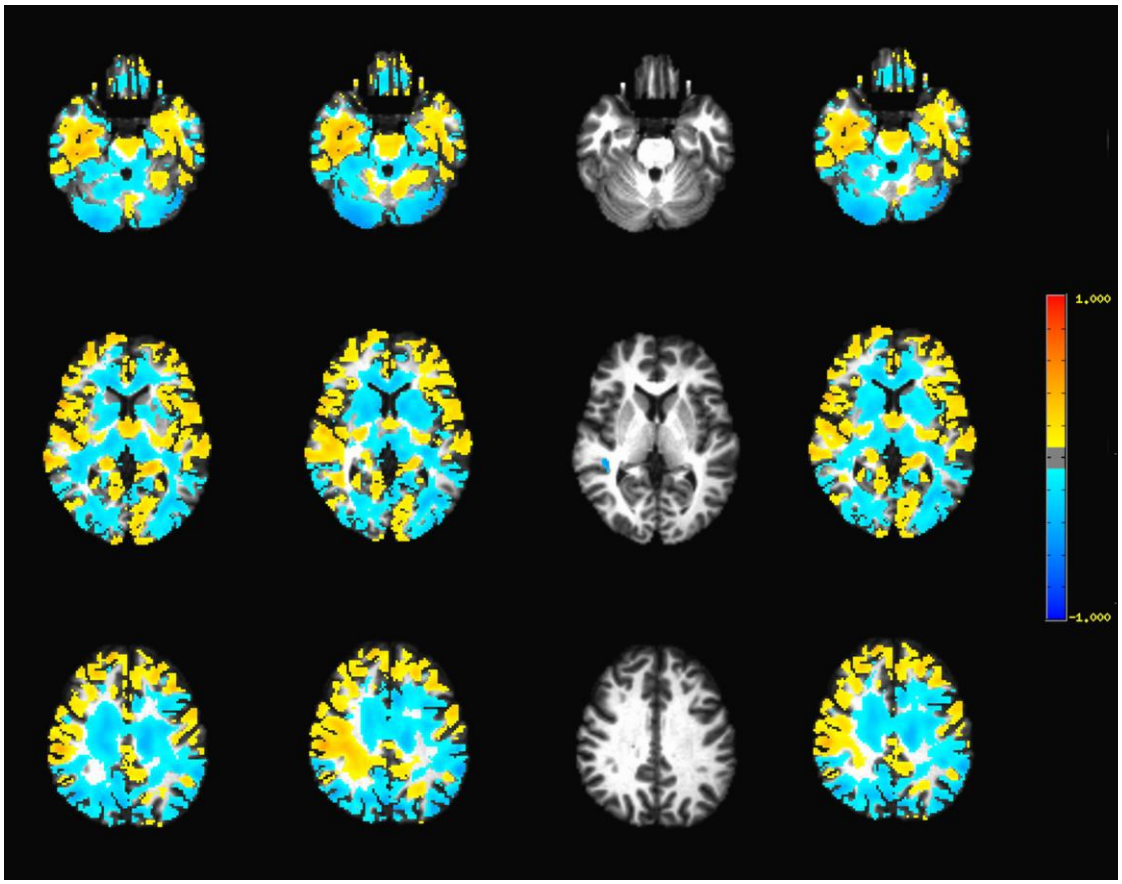

eFigure 15: MD analysis of patients compared to different control cohorts. ComBat harmonization has been applied to each of the control sets. From left to right, we report statistically unthresholded effect sizes of the Mann-Whitney U test on MD of (column 1) patients vs control group 1; (column 2) patients vs control group 2 ; (column 3) control group 1 vs control group 2, $p < 0.05$, uncorrected; and (column 4) patients vs the whole control cohort.

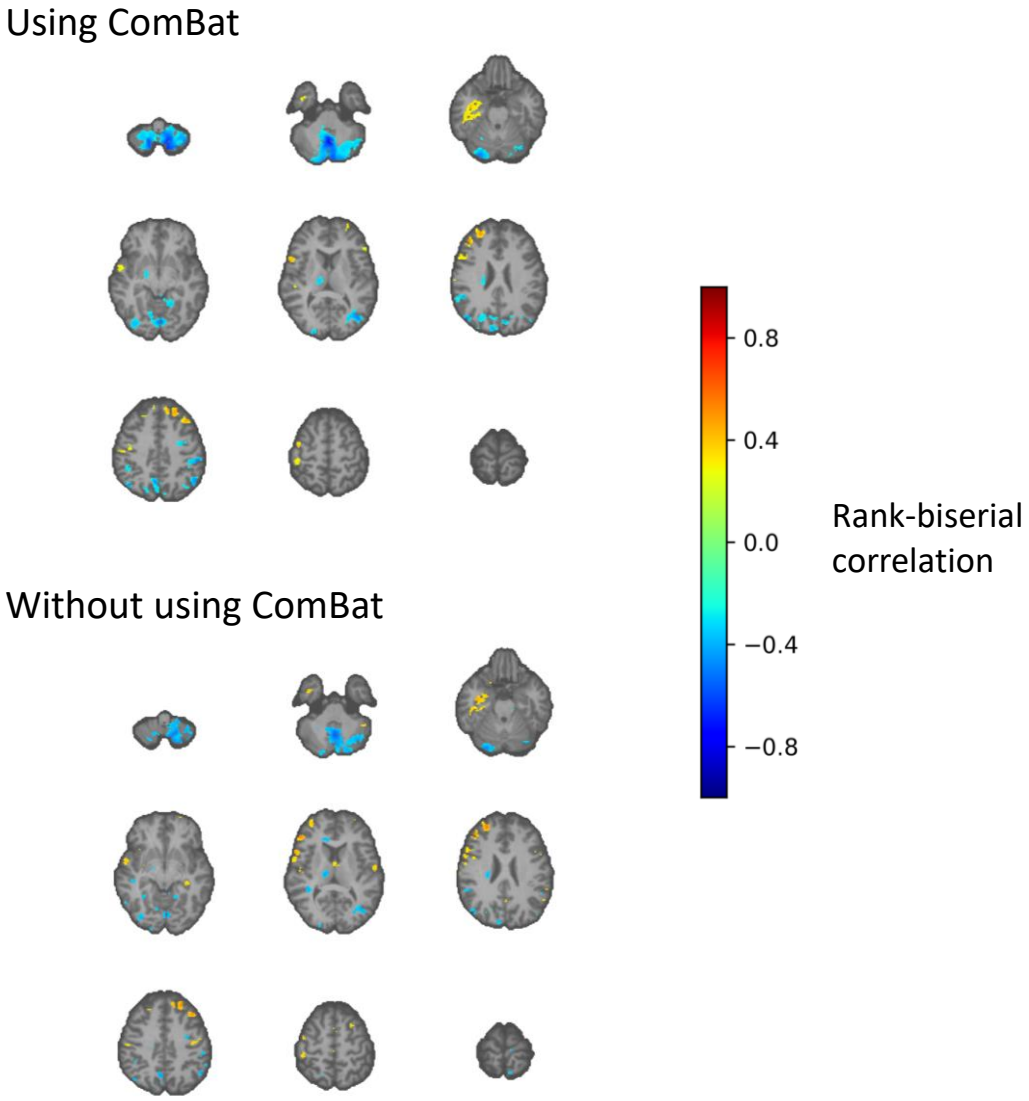

eFigure 16: Comparison of voxelwise MD group comparison with and without ComBat harmonization. The results of Mann-Whitney U test are shown where $p<0.05$ uncorrected. 37 patients were compared against 41 controls using ComBat, and 21 controls without ComBat. Results demonstrate that effect sizes and locations of group difference are very similar between the two tests, but the extent of locations satisfying $p<0.05$ is increased using ComBat, as that test has superior power.

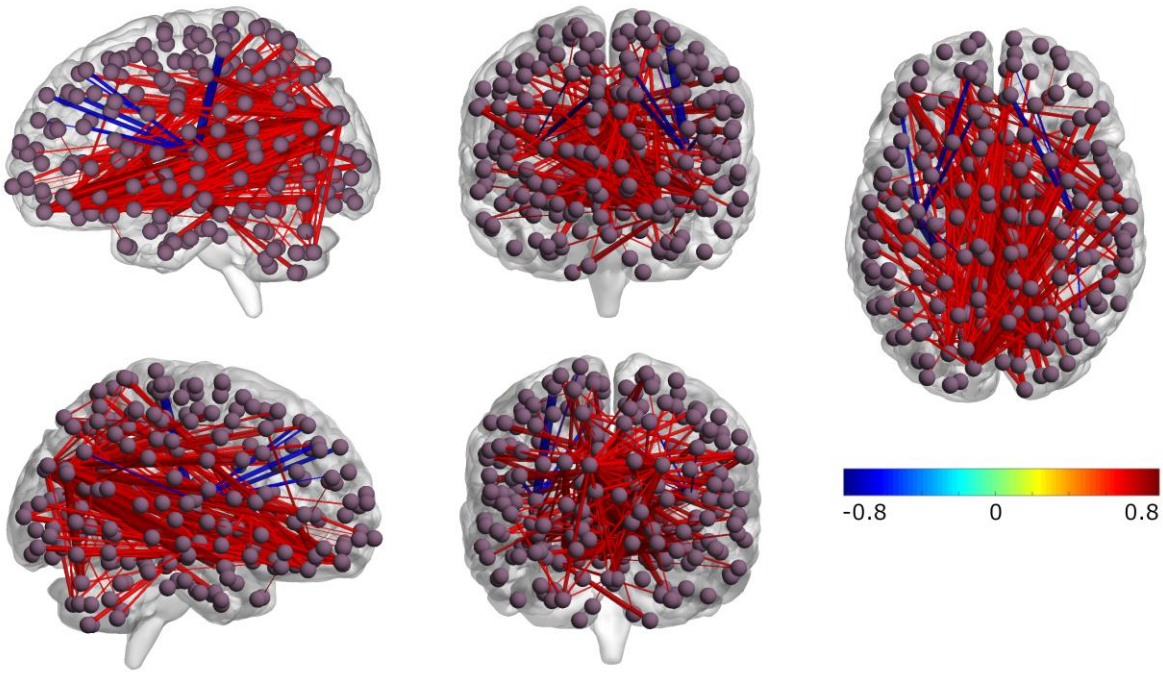

eFigure 17: Structural connectivity analysis of the brain, with the color bar indicating effect size of difference between patients and controls. The whole structural connectome was interrogated at the level of each connection. Edges with $p<0.05$ are shown, not FDR corrected.

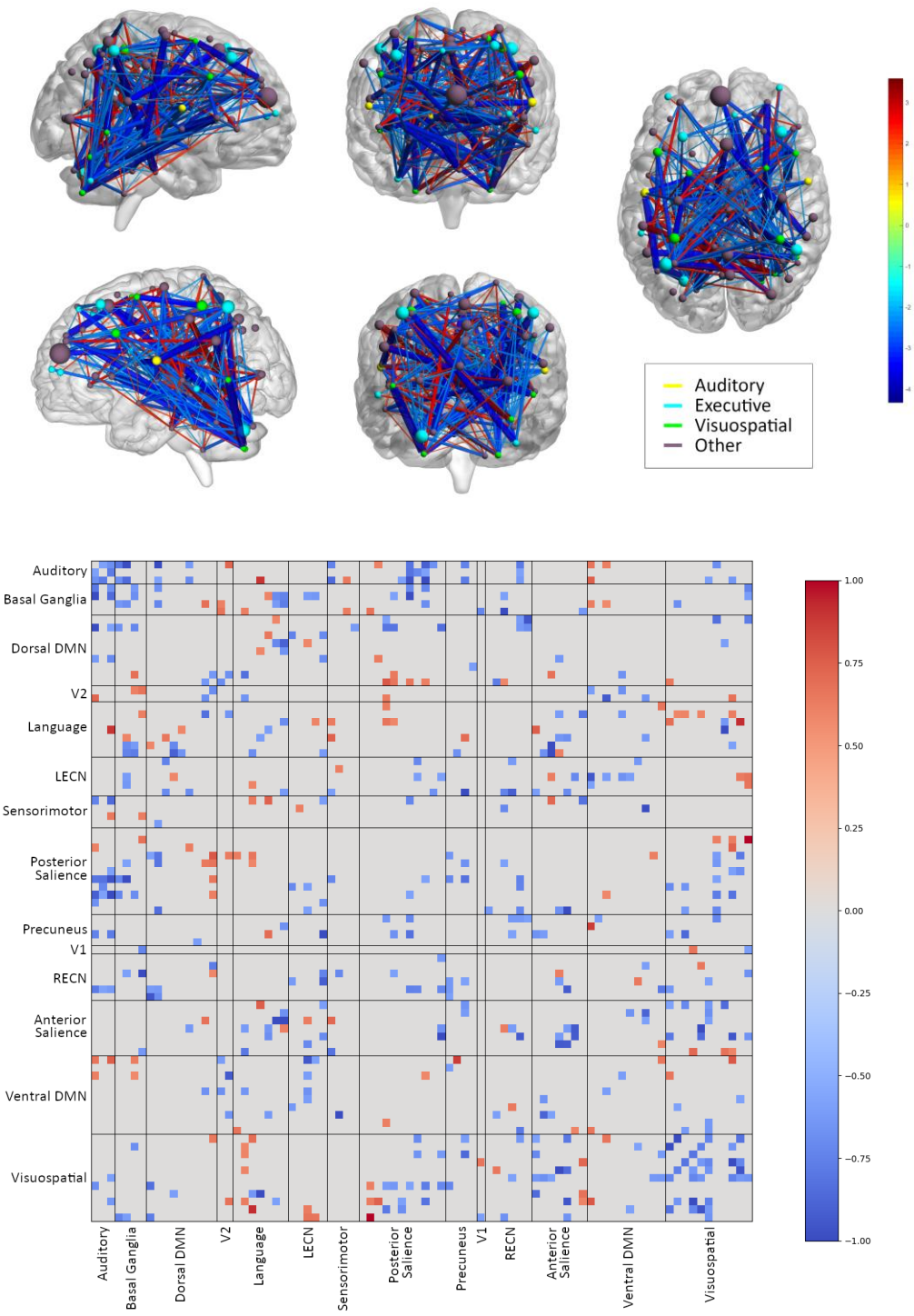

eFigure 18: Analysis of full brain functional connectivity of patients as compared to controls: (Top) Brain representation with the nodes color-coded based on the subnetworks that they are involved in, with the color bar showing the t-statistic of the difference; (Bottom) Matrix representation of the connectome, with the regions grouped on the basis of subnetworks, and color-coded with effect size.

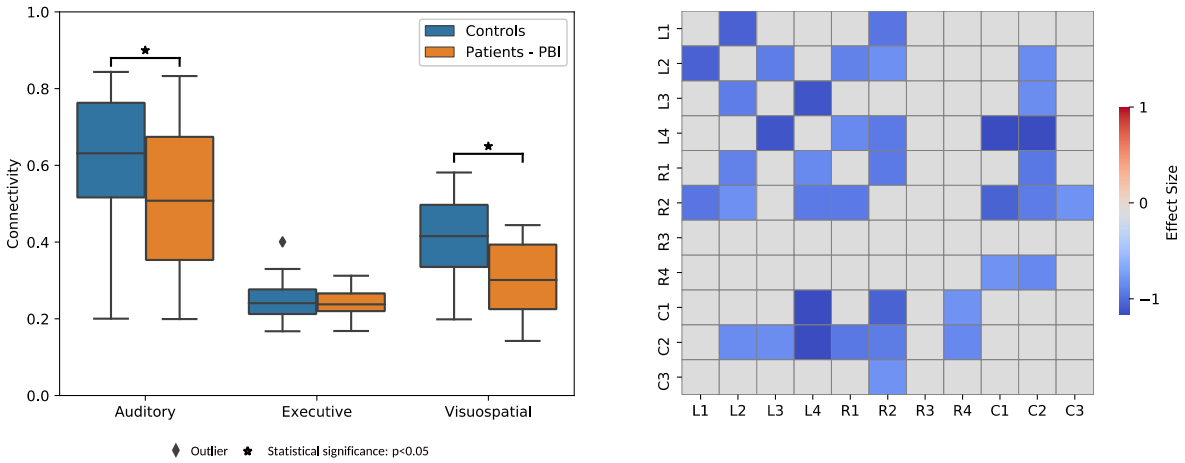

eFigure 19: Differences in functional subnetworks of the patients after excluding the PBI group, as compared to controls: (Left) Differences in the auditory, executive and visuospatial subnetworks. (Right) Effect size of lower connectivity in the visuospatial network presented at the level of regions.

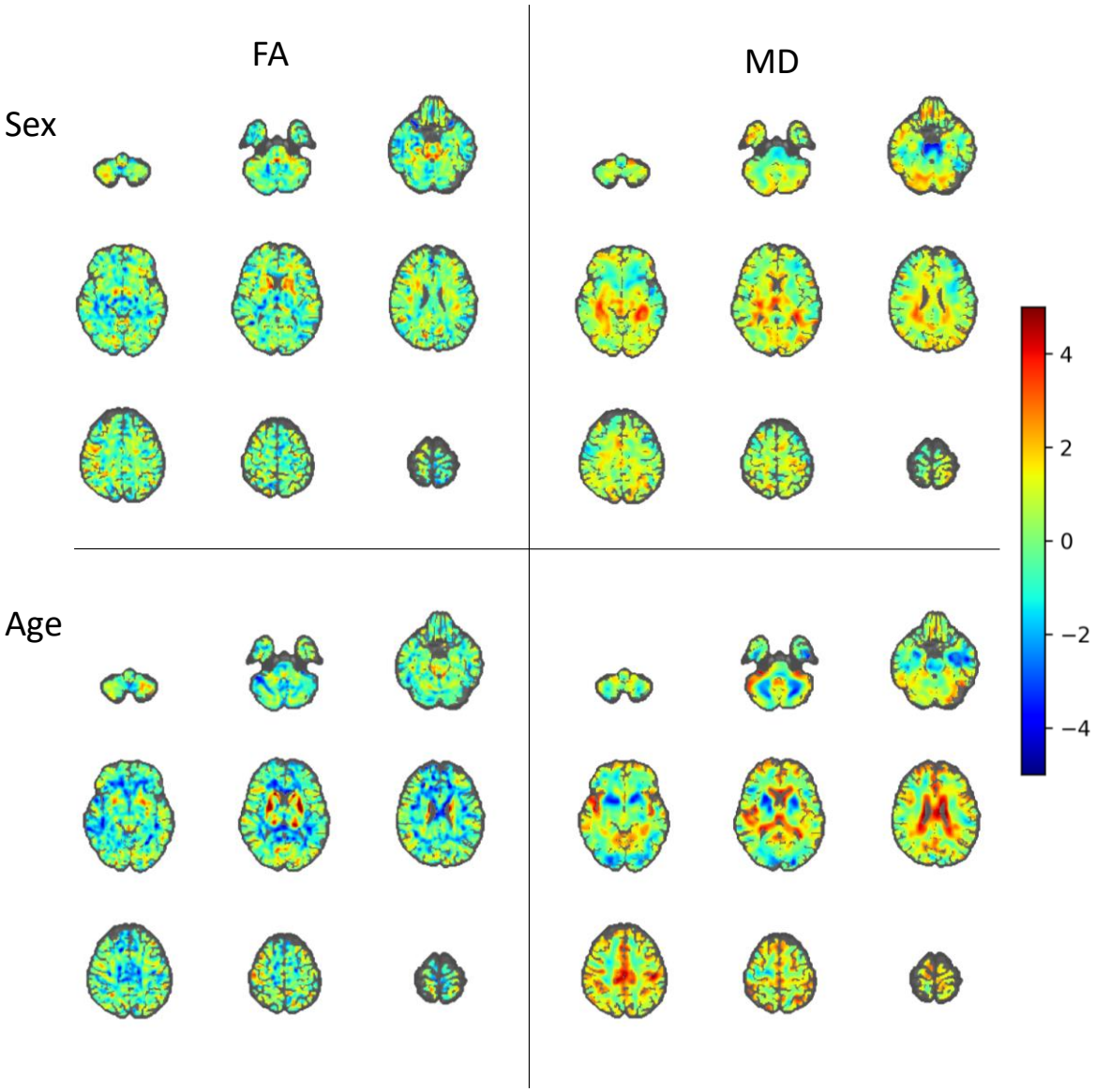

eFigure 20: Age and sex effects in voxel-wise regression analysis of DTI measures. These terms are nuisance variables which were regressed out before a Mann-Whitney U test was run on the residuals of the model. Effects are displayed on 9 axial slices of the template covering entire brain, using the unthresholded t-statistic to display the magnitude of the effect. The color bar applies to all images. Clockwise from top left: FA sex effects; MD sex effects; FA age effects; MD age effects.

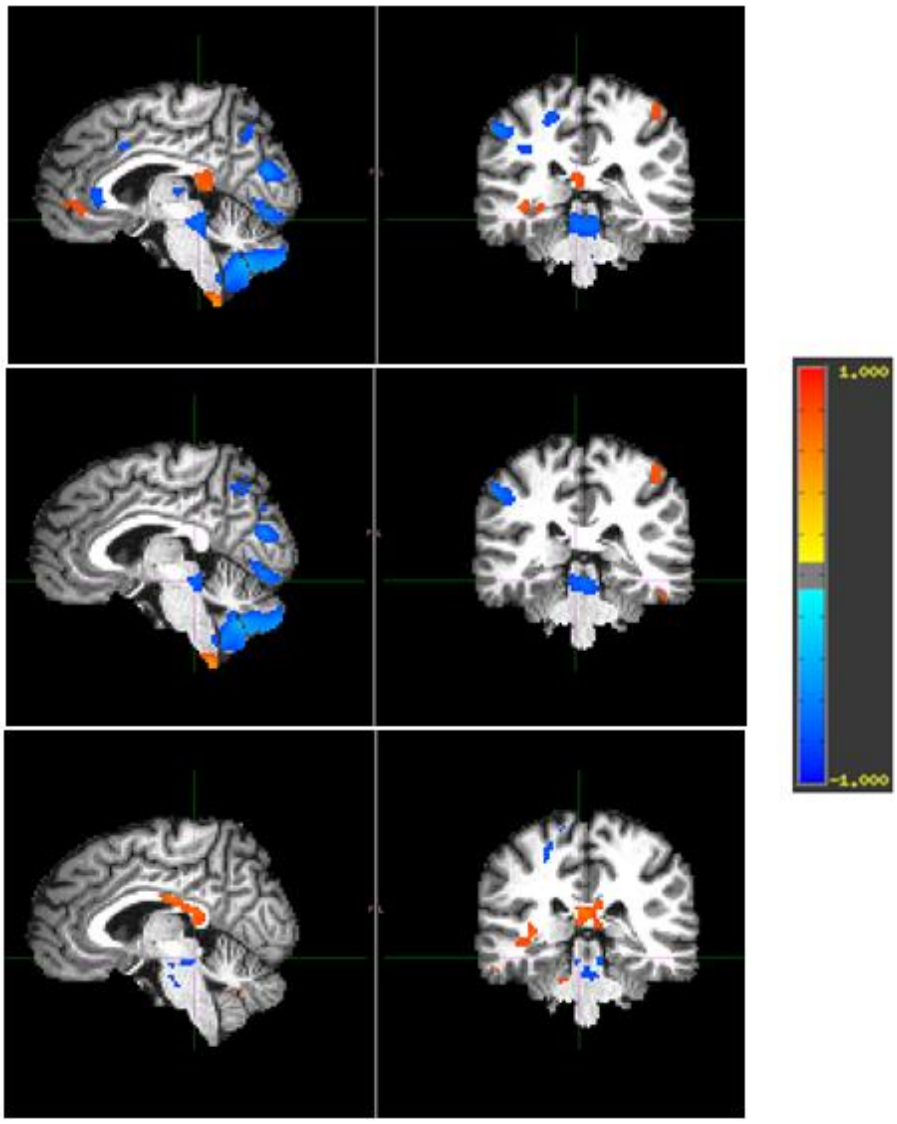

eFigure 21: Additional results of secondary hypothesis of diffusion measures showing differences in patients and controls in additional regions including the inferior colliculi and superior cerebral peduncle in (top) axial diffusivity; (middle) mean diffusivity and (bottom) fractional anisotropy.

eReferences

1. Xu, J., et al., *Evaluation of slice accelerations using multiband echo planar imaging at 3 T.* NeuroImage, 2013. **83**: p. 991-1001.
2. Resnick, S., et al., *Longitudinal changes in MRI volumes in older adults.* Neurobiology of Aging, 2001. **22**(2): p. 332.
3. Resnick, S.M., et al., *Longitudinal Magnetic Resonance Imaging Studies of Older Adults: A Shrinking Brain.* The Journal of Neuroscience, 2003. **23**(8): p. 295-301.
4. Davatzikos C, e.a. *Apolipoprotein E4 Genotype and Longitudinal Changes in Brain Structure in Subsequently Impaired and Cognitively Healthy Older Adults* in *AAIC Annual Conference*. 2018. Chicago, IL.
5. Habes, M., et al., *Advanced brain aging: relationship with epidemiologic and genetic risk factors, and overlap with Alzheimer disease atrophy patterns.* Transl Psychiatry, 2016. **6**: p. e775.
6. Habes, M., et al., *Relationship between APOE Genotype and Structural MRI Measures throughout Adulthood in the Study of Health in Pomerania Population-Based Cohort.* AJNR Am J Neuroradiol, 2016. **37**(9): p. 1636-42.
7. Habes, M., et al., *White matter hyperintensities and imaging patterns of brain ageing in the general population.* Brain, 2016. **139**(Pt 4): p. 1164-79.
8. Ingalhalikar, M., et al., *Diffusion based abnormality markers of pathology: Toward learned diagnostic prediction of ASD.* Neuroimage, 2011. **57**(3): p. 918-927.
9. Ingalhalikar, M., et al., *Sex differences in the structural connectome of the human brain.* Proc Natl Acad Sci U S A, 2014. **111**(2): p. 823-8.
10. Tunc, B., et al., *Establishing a link between sex-related differences in the structural connectome and behaviour.* Philos Trans R Soc Lond B Biol Sci, 2016. **371**(1688).
11. Rozycki, M., et al., *Multisite Machine Learning Analysis Provides a Robust Structural Imaging Signature of Schizophrenia Detectable Across Diverse Patient Populations and Within Individuals.* Schizophr Bull, 2017.
12. Erus, G., et al., *Imaging Patterns of Brain Development and their Relationship to Cognition.* Cerebral Cortex, 2014.
13. Kim, J., et al., *Disrupted structural connectome is associated with both psychometric and real-world neuropsychological impairment in diffuse traumatic brain injury.* J Int Neuropsychol Soc, 2014. **20**(9): p. 887-96.
14. Solmaz, B., et al., *Assessing connectivity related injury burden in diffuse traumatic brain injury.* Hum Brain Mapp, 2017. **38**(6): p. 2913-2922.
15. Tunc, B., et al., *Individualized Map of White Matter Pathways: Connectivity-Based Paradigm for Neurosurgical Planning.* Neurosurgery, 2016. **79**(4): p. 568-577.
16. Erus, G., et al., *Spatial patterns of structural brain changes in type 2 diabetic patients and their longitudinal progression with intensive control of blood glucose.* Diabetes Care, 2015. **38**(1): p. 97-104.
17. Hartung, E.A., et al., *Brain Magnetic Resonance Imaging Findings in Children and Young Adults With CKD.* Am J Kidney Dis, 2018.
18. Sled, J.G., A.P. Zijdenbos, and A.C. Evans, *A nonparametric method for automatic correction of intensity nonuniformity in MRI data.* IEEE Trans Med Imaging, 1998. **17**(1): p. 87-97.
19. Doshi, J., et al., *MUSE: MUlti-atlas region Segmentation utilizing Ensembles of registration algorithms and parameters, and locally optimal atlas selection.* Neuroimage, 2016. **127**: p. 186-195.
20. Manjon, J.V., et al., *Diffusion weighted image denoising using overcomplete local PCA.* PLoS One, 2013. **8**(9): p. e73021.

21. Jenkinson, M., et al., *FSL.* NeuroImage, 2012. **62**(2): p. 782-90.
22. Andersson, J.L.R. and S.N. Sotiropoulos, *An integrated approach to correction for off-resonance effects and subject movement in diffusion MR imaging.* Neuroimage, 2016. **125**: p. 1063-1078.
23. Smith, S.M., *Fast robust automated brain extraction.* Human Brain Mapping, 2002. **17**(3): p. 143-155.
24. Satterthwaite, T.D., et al., *An improved framework for confound regression and filtering for control of motion artifact in the preprocessing of resting-state functional connectivity data.* Neuroimage, 2013. **64**: p. 240-56.
25. Goldszal, A.F., et al., *An image processing protocol for the analysis of MR images from an elderly population.* Journal of Computer Assisted Tomography, 1998. **22**(5): p. 827-837.
26. Davatzikos, C., et al., *Voxel-based morphometry using the RAVENS maps: methods and validation using simulated longitudinal atrophy.* Neuroimage, 2001. **14**(6): p. 1361-9.
27. Misra, C., Y. Fan, and C. Davatzikos, *Baseline and longitudinal patterns of brain atrophy in MCI patients, and their use in prediction of short-term conversion to AD: Results from ADNI.* Neuroimage, 2009. **44**(4): p. 1415-1422.
28. Davatzikos, C., et al., *Longitudinal progression of Alzheimer's-like patterns of atrophy in normal older adults: the SPARE-AD index.* Brain, 2009. **132**(Pt 8): p. 2026-35.
29. Driscoll, I., et al., *Midlife obesity and trajectories of brain volume changes in older adults.* Hum Brain Mapp, 2012. **33**(9): p. 2204-10.
30. Ou, Y., et al., *DRAMMS: Deformable registration via attribute matching and mutual-saliency weighting.* Med Image Anal, 2011. **15**(4): p. 622-39.
31. Basser, P.J. and D.K. Jones, *Diffusion-tensor MRI: theory, experimental design and data analysis - a technical review.* NMR Biomed, 2002. **15**(7-8): p. 456-67.
32. Basser, P.J., J. Mattiello, and D. Le Bihan, *MR diffusion tensor spectroscopy and imaging.* Biophysical Journal, 1994. **66**(1): p. 259-267.
33. Basser, P.J. and C. Pierpaoli, *Microstructural and physiological features of tissues elucidated by quantitative-diffusion-tensor MRI.* Journal of Magnetic Resonance, Series B, 1996. **111**(3): p. 209-219.
34. Pierpaoli, C., et al., *Diffusion tensor MR imaging of the human brain.* Radiology, 1996. **201**(3): p. 637-48.
35. Pierpaoli, C. and P.J. Basser, *Toward a quantitative assessment of diffusion anisotropy.* Magn Reson Med, 1996. **36**(6): p. 893-906.
36. Pasternak, O., et al., *Free water elimination and mapping from diffusion MRI.* Magnetic resonance in medicine : official journal of the Society of Magnetic Resonance in Medicine / Society of Magnetic Resonance in Medicine, 2009. **62**: p. 717-30.
37. Ismail, A.A.O., et al., *Characterizing Peritumoral Tissue Using Free Water Elimination in Clinical DTI*, in *MICCAI 2018 - 21st International Conference on Medical Image Computing and Computer Assisted Intervention ; Workshop : Brain Lesion, Lecture Notes in Computer Science*. Sep, 2018, Springer Granada, Spain. p. in press.
38. Wallace, E.J., J.L. Mathias, and L. Ward, *Diffusion tensor imaging changes following mild, moderate and severe adult traumatic brain injury: a meta-analysis.* Brain Imaging and Behavior, 2018: p. 1-15.
39. Shenton, M.E., et al., *A Review of Magnetic Resonance Imaging and Diffusion Tensor Imaging Findings in Mild Traumatic Brain Injury.* Brain Imaging Behav., 2012. **6**(2): p. 137–192
40. Rovaris, M., et al., *Diffusion MRI in multiple sclerosis.* Neurology, 2005. **65**(10): p. 1526-1532.
41. Filippi, M., et al., *Diffusion tensor magnetic resonance imaging in multiple sclerosis.* Neurology, 2001. **56**(3): p. 304-311.

42. Sullivan, E.V. and A. Pfefferbaum, *Diffusion tensor imaging and aging.* Neuroscience and Biobehavioral Reviews, 2006. **30**(6): p. 749-761.
43. Madden, D.J., et al., *Diffusion tensor imaging of cerebral white matter integrity in cognitive aging.* Biochim Biophys Acta, 2011. **1822**(3): p. 386-400. .
44. Sullivan, E.V. and A. Pfefferbaum, *Diffusion tensor imaging in normal aging and neuropsychiatric disorders.* European Journal of Radiology, 2003. **45**(3): p. 244-255.
45. Whitford, T.J., M. Kubicki, and M.E. Shenton, *Diffusion tensor imaging, structural connectivity, and schizophrenia.* Schizophr Res Treatment, 2011.
46. Kubicki, M., et al., *A review of diffusion tensor imaging studies in schizophrenia.* Journal of Psychiatric Research, 2007. **41**(1-2): p. 15-30.
47. Schaefer, P.W., P.E. Grant, and R.G. Gonzalez, *Diffusion-weighted MR Imaging of the Brain* Radiology 2000.
48. Bendlin, B., et al., *Longitudinal changes in patients with traumatic brain injury assessed with diffusion tensor and volumetric imaging.* Neuroimage, 2008. **42**(2): p. 503-514.
49. Basser, P.J., et al., *In vivo fiber tractography using DT-MRI data.* Magnetic Resonance in Medicine, 2000. **44**(4): p. 625-632.
50. Wakana, S., et al., *Fiber Tract-based Atlas of Human White Matter Anatomy.* Radiology, 2004. **230**(1): p. 77-87.
51. Hagmann, P., et al., *MR connectomics: Principles and challenges.* J Neurosci Methods, 2010. **194**(1): p. 34-45.
52. Hagmann, P., et al., *Mapping the structural core of human cerebral cortex.* PLoS Biol, 2008. **6**(7): p. e159.
53. Verde, A.R., et al., *UNC-Utah NA-MIC framework for DTI fiber tract analysis.* Frontiers in neuroinformatics, 2014. **7**: p. 51.
54. Garyfallidis, E., et al., *Dipy, a library for the analysis of diffusion MRI data.* Front Neuroinform, 2014. **8**(8): p. 8.
55. Daducci, A., et al., *The Connectome Mapper: An Open-Source Processing Pipeline to Map Connectomes with MRI.* 2012. **7**(12): p. e48121.
56. Yeo, B.T.T., et al., *The organization of the human cerebral cortex estimated by intrinsic functional connectivity.* J Neurophysiol, 2011. **106**(3): p. 1125-65.
57. Avants, B.B., N.J. Tustison, and H.J. Johnson. *ANTs Distribution, http://stnava.github.io/ANTs/*. Available from: http://stnava.github.io/ANTs/.
58. Avants, B.B., et al., *The Insight ToolKit image registration framework.* Frontiers in neuroinformatics, 2014. **8**(44).
59. Behrens, T.E., et al., *Probabilistic diffusion tractography with multiple fibre orientations: What can we gain?* Neuroimage, 2007. **34**(1): p. 144-55.
60. Shirer, W.R., et al., *Decoding subject-driven cognitive states with whole-brain connectivity patterns.* Cerebral Cortex 2012.
61. Mori, S., K. Oishi, and E. al., *Stereotaxic white matter atlas based on diffusion tensor imaging in an ICBM template.* Neuroimage, 2008. **40**(2): p. 570-582.
62. Mori, S., S. Wakana, and P.C. Van Zijl, *MRI atlas of human white matter*. 1st ed. 2005, Amsterdam ; Boston: Elsevier. viii, 239 p.
63. Fortin, J.P., et al., *Harmonization of multi-site diffusion tensor imaging data.* Neuroimage, 2017. **161**: p. 149-170.
64. Tustison, N.J., et al., *N4ITK: Improved N3 Bias Correction.* IEEE Transactions on Medical Imaging, 2010. **29**(6): p. 1310-1320.
65. Neuromorphometrics. *Multi Subject Atlas using Brain Color labeling protocol* 2012; Available from: https://scalablebrainatlas.incf.org/human/NMM1103.

66. Reardon, P.K., et al., *Normativebrain size variation and brain shapediversity in humans.* Science, 2018. **360**: p. 1222–1227.
67. Oishi, K., A.V. Faria, and S. Mori. *JHU-MNI-ss Atlas*. Department of Radiology 2010; Available from: https://github.com/Jfortin1/EveTemplate.
68. Swanson III, R.L., et al., *Neurological manifestations among us government personnel reporting directional audible and sensory phenomena in Havana, cuba.* JAMA, 2018. **319**(11): p. 1125-1133.
69. Wardlaw, J.M., M.C.V. Hernandez, and S. Munoz-Maniega, *What are White Matter Hyperintensities Made of? Relevance to Vascular Cognitive Impairment.* Journal of the American Heart Association, 2019.
70. Fazekas, F., et al., *MR signal abnormalities at 1.5 T in Alzheimer's dementia and normal aging.* AJR Am J Roentgenol. , 1987. **149**(2): p. 351-6.
71. Kim, K.W., J.R. MacFall', and M.E. Payne, *Classification of white matter lesions on magnetic resonance imaging in the elderly.* Biol Psychiatry, 2008 **54**(4): p. 273–280.
72. Alahmari, K.A., et al., *Estimating postural control with the balance rehabilitation unit: measurement consistency, accuracy, validity, and comparison with dynamic posturography.* Archives of physical medicine and rehabilitation, 2014. **95**: p. 65-73.
73. Gallaway, M., M. Scheiman, and G.L. Mitchell, *Vision Therapy for Post-Concussion Vision Disorders.* Optometry and vision science : official publication of the American Academy of Optometry, 2017. **94**: p. 68-73.
74. Scheiman, M. and B. Wick, *Clinical Management of Binocular Vision: Heterophoric, Accommodative and Eye Movement Disorders.,* . 4th ed. 2014, Philadelphia, PA: Lippincott Williams & Wilkins
75. Garzia, R.P., et al., *A new visual-verbal saccade test: the development eye movement test (DEM).* Journal of the American Optometric Association 1990. **61**: p. 124-35.